Local Helioseismology: Three-Dimensional Imaging of the Solar Interior

Laurent Gizon,[1] Aaron C. Birch,[2] and Henk C. Spruit[3]

[1]Max-Planck-Institut für Sonnensystemforschung, 37191 Katlenburg-Lindau, Germany;
email: gizon@mps.mpg.de

[2]NorthWest Research Associates, Colorado Research Associates Division, Boulder,
Colorado 80301; email: aaronb@cora.nwra.com

[3]Max-Planck-Institut für Astrophysik, 85748 Garching, Germany;
email: henk@mpa-garching.mpg.de

Key Words

solar convection, solar cycle, solar magnetism, solar oscillations, sunspots

Abstract

The Sun supports a rich spectrum of internal waves that are continuously excited by turbulent convection. The Global Oscillation Network Group (GONG) network and the SOHO/MDI (*Solar and Heliospheric Observatory/ Michelson Doppler Imager*) space instrument provide an exceptional database of spatially resolved observations of solar oscillations, covering more than an entire sunspot cycle (11 years). Local helioseismology is a set of tools for probing the solar interior in three dimensions using measurements of wave travel times and local mode frequencies. Local helioseismology has discovered (*a*) near-surface vector flows associated with convection, (*b*) 250 m s^{-1} subsurface horizontal outflows around sunspots, (*c*) ∼50 m s^{-1} extended horizontal flows around active regions (converging near the surface and diverging below), (*d*) the effect of the Coriolis force on convective flows and active region flows, (*e*) the subsurface signature of the 15 m s^{-1} poleward meridional flow, (*f*) a ±5 m s^{-1} time-varying depth-dependent component of the meridional circulation around the mean latitude of activity, and (*g*) magnetic activity on the farside of the Sun.

1. INTRODUCTION

Active region: region of enhanced magnetic activity, including sunspots and diffuse magnetic field (plage)

Helioseismology is the observation and interpretation of the solar oscillations to probe the solar interior. These oscillations, with periods around 5 min, are due to the random superposition of acoustic waves and surface-gravity waves and are excited by turbulent convection in the upper layers of the Sun. Solar oscillations were discovered by Leighton, Noyes & Simon (1962) and interpreted by Ulrich (1970) and Leibacher & Stein (1971) as internal acoustic waves trapped in spherical-shell cavities. Wave motions are measured along the line of sight from the Doppler shifts of absorption lines in the solar spectrum. A short review of solar oscillations is given in Section 2.

Helioseismology has produced a large number of discoveries in solar, stellar, and fundamental physics. It provides the most precise tests of the theory of stellar structure and evolution; for example, it motivated a revision of the standard model of particle physics to solve the solar neutrino problem. Helioseismology also enables the study and discovery of effects that are not included in standard solar models (standard models are spherically symmetric, nonrotating, and nonmagnetic, and include a simplified treatment of convection).

One of the most exciting aspects of helioseismology is the search for the origin of the Sun's magnetic field, which is one of the most important unsolved problems in solar physics. The 11-year solar magnetic cycle is thought to be due to a field-amplification (dynamo) process (cf. Charbonneau 2005, Rempel 2008), whereby a toroidal magnetic field component (in the azimuthal direction with respect to the rotation axis) is built up by stretching of the field lines by the Sun's differential rotation. In a second step, the toroidal field is partially converted into a poloidal field component, which "closes" the dynamo cycle. Models for this second step ("α-effect") differ significantly. In most models, it is attributed to the effect of convection on the magnetic field (convective dynamos). In an older model more closely connected with observations, convective flows play no role in this step; it is instead due to the instability of the toroidal field itself. The instability causes loops of magnetic field to rise to the solar surface and appear as the observed magnetic (sunspot) activity. Resolution of this conflict between the models is key for progress toward a theory of stellar magnetic fields that has real predictive power. Helioseismology holds the promise of providing new observational constraints on cycle-related structures below the surface (e.g., Kosovichev 2008).

Traditionally, helioseismology methods have been classified into two groups: global helioseismology and local helioseismology. Global helioseismology consists of measuring the frequencies of the modes of oscillation and searching for seismic solar models whose oscillation frequencies match the observed ones (see Christensen-Dalsgaard 2002 for a review of techniques and results). Global helioseismology is two dimensional and is used to infer solar properties as functions of radius and unsigned latitude. A major achievement of global helioseismology is the inference of the angular velocity in the solar interior (e.g., Schou et al. 1998, Thompson et al. 2003). The differentially rotating convection zone and the rigidly rotating radiative interior are separated by a transition region at $0.69\,R_\odot$, the tachocline, which may be the seat of the solar dynamo.

Unlike standard global mode helioseismology, local helioseismology is capable of probing the solar interior in three dimensions. This is important for the study of solar activity, which is seen on the surface as localized patches of magnetic field, e.g., active regions, sunspots, and plage regions. Local helioseismology can potentially be used to infer vector flows, thermal and structural inhomogeneities, and even the magnetic field itself. Local helioseismology has been reviewed by e.g., Kosovichev & Duvall (1997), Braun & Lindsey (2000), Kosovichev, Duvall & Scherrer (2000), Christensen-Dalsgaard (2002), Kosovichev et al. (2002), Komm, Howe & Hill (2006), Gizon & Thompson (2007), Birch (2008), and Thompson & Zharkov (2008). The most comprehensive review is provided by Gizon & Birch (2005).

Local helioseismology encompasses various methods of data analysis (Section 3). One method of local helioseismology, ring-diagram analysis, is a relatively straight-forward extension of global helioseismology. It consists of measuring local frequencies of oscillation by analyzing small patches on the Sun. Ring-diagram analysis is computationally efficient and has produced important results, such as maps of flow patterns in the Sun.

Other methods of local helioseismology, like time-distance helioseismology and helioseismic holography, are based on the computation of the cross-covariance between the oscillation signal measured at two points on the surface. The basic principle is to retrieve information about the solar interior from the time it takes for solar waves to travel between any two surface locations through the solar interior. The cross-covariance function is directly related to the Green's function and thus carries essential information.

As in global helioseismology, an inverse problem must be solved in order to retrieve subsurface solar properties from local helioseismic measurements (Section 4). In many cases it is acceptable to assume that the Sun is weakly heterogeneous in the horizontal directions: the inverse problem becomes a linear inverse problem and can be solved with standard techniques. However, this is not always possible, especially in the presence of strong magnetic fields, e.g., in a sunspot.

Time-distance helioseismology aims at inferring subsurface properties at the best spatial and temporal resolution possible. A spatial resolution as high as a few megameters can be achieved near the surface. This limit is intimately linked to the smallest available horizontal wavelength of the solar oscillations (high-frequency surface gravity waves). Detailed 3D maps of vector flows in the upper convection zone have provided new insights into the structure, evolution, and organization of magnetic active regions and convective flows. The most easily detectable flow pattern is supergranulation, an intermediate scale of convection (Section 5).

A particularly challenging aspect of local helioseismology is sunspot helioseismology (Section 6). Sunspots are regions of intense (kilogauss) magnetic field and low gas pressure and density. In spite of an abundance of telling clues from observations of the solar surface, theories about sunspot formation, subsurface structure, thermal properties, and deep magnetic field topology are still controversial. The nature of solar waves is very significantly altered as they propagate through a sunspot and convert into magneto-acoustic-gravity (MAG) waves. Numerical models of wave propagation through sunspots are currently being developed by several groups. These simulations will be key to interpreting the solar oscillations in the vicinity of sunspots. Realistic numerical simulations also promise to be an important diagnostic tool for sunspot structure. The main question—What keeps a sunspot together as a clearly delineated entity?—may not ultimately be answerable by helioseismology, because key elements of the answer may well lie in a region near the base of the convection zone, where helioseismological tools may not have enough sensitivity to detect a sunspot-related signal. They may perhaps be sufficient, however, to challenge models that propose the origin of sunspots to be in the surface layers. (Section 7 discusses the discovery of extended flows around large complexes of magnetic activity and their relation to the solar cycle.)

Among the most interesting results of local helioseismology is the detection of the subsurface meridional flow (Section 8). The meridional flow does not affect global mode frequencies (to first order), and thus has only been measured in the solar interior with local helioseismology. The meridional flow plays an important role in "flux transport" theories, according to which the latitudinal transport of magnetic flux at the base of the convection zone determines the period of the solar cycle.

In yet another remarkable application, local helioseismology can be used to construct maps of active regions on the farside of the Sun (Section 9). In farside imaging, the Sun as a whole is used as an acoustic lens focusing waves at a point on the invisible hemisphere. Maps of the farside are potentially important to predict space weather and provide advance warning for coronal mass

Ring-diagram analysis: analysis of the local frequencies of solar oscillations over small patches of the solar disk

Cross-covariance: measure of similarity of two random signals as a function of a time lag applied to one of them

Inverse problem: the problem of inferring solar subsurface properties from helioseismology measurements

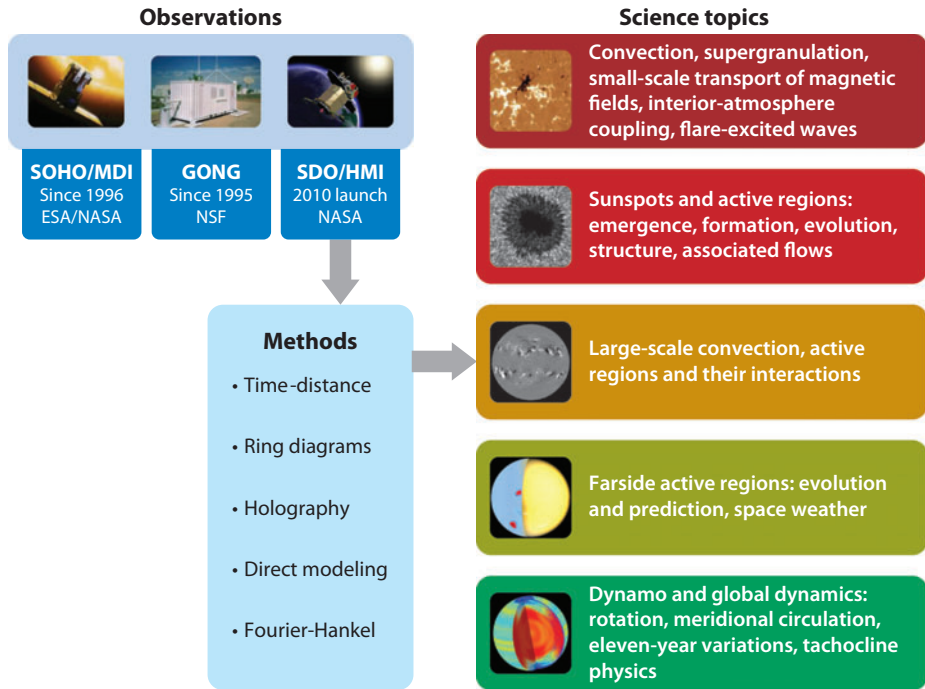**Farside:** side of the Sun that is not visible from the Earth

Observations

SOHO/MDI Since 1996 ESA/NASA	**GONG** Since 1995 NSF	**SDO/HMI** 2010 launch NASA

Methods

- Time-distance
- Ring diagrams
- Holography
- Direct modeling
- Fourier-Hankel

Science topics

Convection, supergranulation, small-scale transport of magnetic fields, interior-atmosphere coupling, flare-excited waves

Sunspots and active regions: emergence, formation, evolution, structure, associated flows

Large-scale convection, active regions and their interactions

Farside active regions: evolution and prediction, space weather

Dynamo and global dynamics: rotation, meridional circulation, eleven-year variations, tachocline physics

Figure 1

Overview of local helioseismology: observational data, methods of analysis, and scientific applications.

ejections and solar flares (violent and sudden releases of energy associated with the reconfiguration of the magnetic field in the atmosphere above an active region). Flares can excite acoustic waves to measurable levels, which can in turn tell us about the physics of flares (Section 10).

These examples illustrate the many facets of the science possible with local helioseismology, as summarized in **Figure 1**. In all these cases, a taste of the possibilities has been provided, but improved observations (Section 11) and further developments in the techniques of analysis and interpretation are required to realize the full potential of local helioseismology.

2. SOLAR OSCILLATIONS

2.1. Observations

In most cases, local helioseismology uses time series of Dopplergrams as input data. A Dopplergram is a digitized image of the line-of-sight velocity of the solar surface (photosphere or chromosphere) deduced from the Doppler shifts of a Fraunhofer absorption line (e.g., Scherrer et al. 1995). Solar oscillations have a higher signal-to-noise ratio in Doppler velocity than in intensity, especially at low frequencies.

There are two major data sets available for local helioseismology. The first one is provided by the Global Oscillation Network Group (GONG) (Harvey et al. 1996), headquartered in Tucson, Arizona, which operates a global network of six stations around the world. The sites are distributed in longitude in order to observe continuously: Big Bear (California), Mauna Loa (Hawaii), Learmonth (Australia), Udaipur (India), El Teide (Canary Islands), and Cerro Tololo (Chile). The cadence of the observations is one minute to avoid temporal aliasing. Each GONG instrument is a

Dopplergram: image of the line-of-sight component of velocity of the solar surface

phase-shift interferometer that measures the phase of the Fourier transform of the solar spectrum around the Ni absorption line at 6768 Å, interpreted as a Doppler shift (Harvey & The GONG Instrument Team 1995). Although the original cameras had an image size of 256×256 pixels, full-disk Dopplergrams have been recorded with $1{,}024 \times 1{,}024$ CCD cameras since 2001, hence providing a good spatial resolution (5 arcsec) for local helioseismology. The GONG instruments also acquire intensity images and line-of-sight magnetograms. The effective duty cycle of the merged observations is over 90%.

The other main data set is provided by the Michelson Doppler Imager (MDI) (Scherrer et al. 1995) on board the ESA/NASA *Solar and Heliospheric Observatory* (SOHO), which was launched in December 1995. SOHO is in a halo orbit around the Sun-Earth L1 Lagrange point. Observations from SOHO are not only continuous, but benefit from perfect seeing and from a slowly varying spacecraft-to-Sun velocity. The MDI filter system relies on two tunable Michelson interferometers in order to measure intensity in five very narrow filters (94 mÅ) in the wings and core of the Ni 6768 line. The Doppler velocity is obtained by taking the difference between filtergrams on each side of the absorption line. The MDI observables are the line depth and continuum, line-of-sight Doppler velocity, and line-of-sight magnetic field. The temporal cadence is one minute and the CCD camera has $1{,}024 \times 1{,}024$ pixels. It can operate in two different modes: a full-disk mode (2 arcsec pixel) or a high-resolution mode (0.6 arcsec pixel). **Figure 2** shows example full-disk SOHO/MDI observables and **Supplemental Video 1** (follow the **Supplemental Material link** from the Annual Reviews home page at **http://www.annualreviews.org**) shows a time series of full-disk Dopplergrams. In high-resolution mode, the resolution is better by a factor of three but the field of view is reduced. Because of limited telemetry, the full-disk Dopplergrams have only been transmitted at full cadence for about two to three months each year since 1996, whereas the high-resolution Dopplergrams are reserved for targeted campaigns of observation. The rest of the time, the Dopplergrams are spatially filtered onboard and converted into lower resolution 256×256 images, in order to save telemetry (medium-degree data).

Supplemental Material

GONG and MDI are complemented by other data sets, e.g., from the Taiwan Oscillation Network (TON) (Chou et al. 1995), from campaigns of observations at the South Pole with the Magneto-Optical filter at Two Heights (MOTH) (Finsterle et al. 2004a), and from the Hinode satellite (e.g., Mitra-Kraev, Kosovichev & Sekii 2008).

In many applications of local helioseismology, the standard procedure consists of choosing a relatively small region of the Sun and following (or tracking) it in a frame that is corotating with the Sun. This gives a time series of Doppler images that are centered on the region of interest, like a magnetic active region. In this process each individual image is mapped onto a common spatial grid.

For local studies, it is often convenient to neglect the curvature of the solar surface and work in plane-parallel geometry. With this simplification, it is natural to study the oscillations in 3D Fourier space. The oscillation signal, denoted by $\phi(\mathbf{r}, t)$, where $\mathbf{r} = (x, y)$ is the horizontal position vector and t is time, is decomposed into harmonic components

$$\phi(\mathbf{k}, \omega) = \int_A \mathrm{d}^2\mathbf{r} \int_0^T \mathrm{d}t \, \phi(\mathbf{r}, t) \, e^{-i\mathbf{k}\cdot\mathbf{r} + i\omega t}, \qquad (1)$$

where A is the area of study, T is the total observation time, the vector $\mathbf{k} = (k_x, k_y)$ is the horizontal wave vector, and ω is the angular frequency. The horizontal wave number is $k = ||\mathbf{k}||$. By convention, the x coordinate is positive in the direction of rotation (prograde) and the y coordinate points north. The power spectrum of solar oscillations is defined as

$$P(\mathbf{k}, \omega) = |\phi(\mathbf{k}, \omega)|^2. \qquad (2)$$
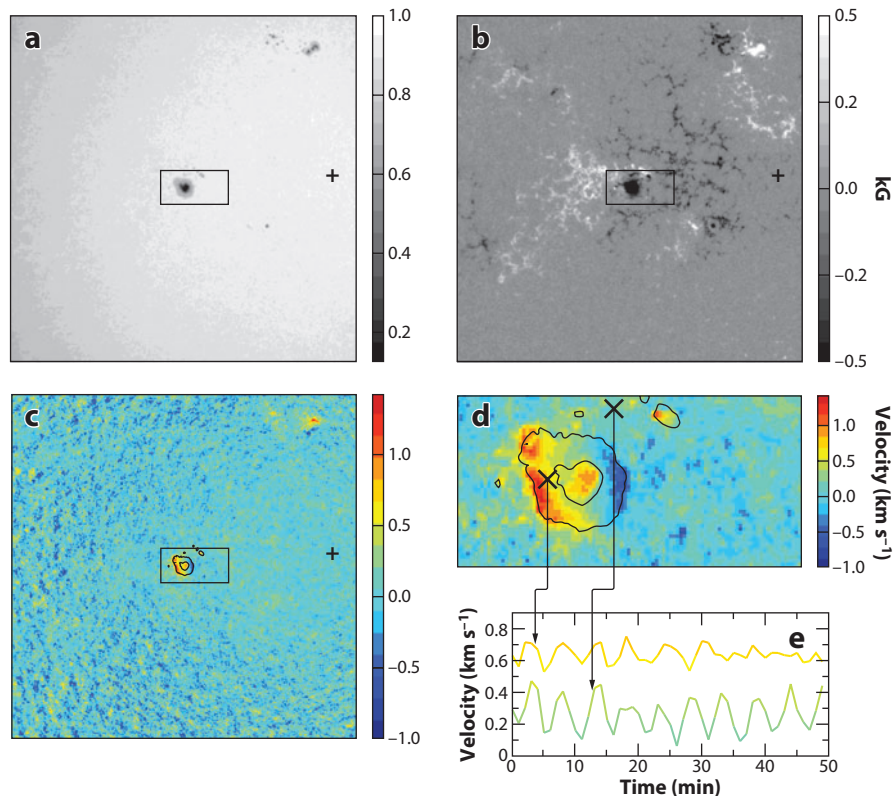
Figure 2

Observations taken by the *Solar and Heliospheric Observatory*/Michelson Doppler Imager on January 22, 2008 at 17:36:00, remapped using Postel's azimuthal equidistant projection with a map scale of 0.12 heliographic degree per pixel or 1.46 Mm pixel^{-1}. The sunspot in Active Region NOAA 9787 is at the center of projection. (*a*) 512 × 512 pixel subfield of the continuum intensity, normalized to unity at disk center (*plus symbol*). The box around the sunspot has size 147 Mm × 73 Mm. (*b*) Line-of-sight component of the magnetic field in kilogauss (truncated *gray scale*). (*c*) Line-of-sight Doppler velocity in kilometers per second. Supergranulation is visible toward the edges of the frame. (*d*) Doppler velocity in the sunspot box. The black contours show the outer edges of the umbra and penumbra of the sunspot. The center-to-disk component of the Evershed outflow is visible in the penumbra. (*e*) Doppler velocity as a function of time at the two locations denoted by the crosses in panel *d*. The 5-min period of the solar oscillations is evident. The oscillations have reduced amplitudes in the sunspot.

We note that the spatial Fourier transform should be replaced by a spherical harmonic transform when curvature effects cannot be ignored, as in global helioseismology.

An example power spectrum of solar oscillations is shown in **Figure 3**. Power is distributed along well-defined discrete ridges in wave number–frequency space and peaks around 3 mHz. The first ridge at low frequencies shows the "fundamental" (f) modes. These are surface gravity waves with exponential eigenfunctions and a dispersion relation $\omega^2 = gk$, where $g = 274$ m s^{-2} is the acceleration of gravity at the solar surface; they are similar to waves at the surface of a deep ocean. All other ridges correspond to pressure (p) modes, i.e., acoustic waves modified by gravity. The existence of discrete ridges, $\omega = \omega_n(k)$ with $n > 0$, reflects the fact that p modes are trapped in the vertical direction. At fixed wave number, the peaks of power are labeled p$_0$, p$_1$, p$_2$, etc. with increasing frequency. A mode p$_n$ is such that the number of radial nodes of the mode displacement
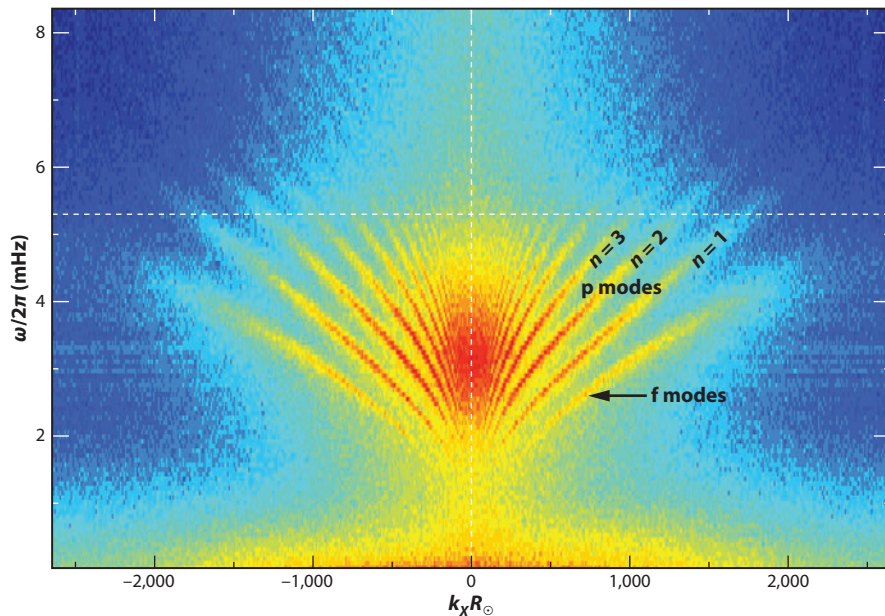
Figure 3

Cut at $k_y = 0$ through an average power spectrum of *Solar and Heliospheric Observatory*/Michelson Doppler Imager high-resolution Doppler velocity data as a function of frequency and $k_x R_\odot$. The horizontal dashed line shows the acoustic cutoff frequency. In order to reduce random noise, an average was carried out over eight individual power spectra, each of duration $T = 4$ hr and covering an apodized region of area $A \sim (500 \text{ Mm})^2$. Because $k_y = 0$, only waves traveling in the east or west directions are shown. The power below $\sim$1.5 mHz is due to solar convection, granulation, and supergranulation.

is n (the radial order). By convention, the f modes are labeled with $n = 0$. All ridges have reduced power above 5.3 mHz, which is the cutoff frequency above which waves are not reflected back into the Sun but escape into the atmosphere. The frequency width of a ridge is inversely proportional to the mode lifetime. A recent description of the mode parameters, including mode lifetimes, is provided by Korzennik, Rabello-Soares & Schou (2004).

2.2. Modes

In order to better understand the diagnostic capability of each mode, it is useful to consider simple solar models. For our purpose, a simple solar model is a reference standard solar model, which only depends on height (or radius), such as Model S (Christensen-Dalsgaard et al. 1996). In plane-parallel models that are isotropic and translation invariant in the horizontal directions, the normal modes of the oscillations of the model vary horizontally as $\exp(i\mathbf{k}\cdot\mathbf{r})$. For the case of p and f modes, it is convenient to introduce the mode eigenfunctions $U_n(z; k)$ and $V_n(z; k)$ such that the complex displacement eigenfunction of the mode characterized by radial order n and horizontal wavevector $\mathbf{k}$ is

$$\boldsymbol{\xi}_n(\mathbf{r}, z; \mathbf{k}) = [\hat{\mathbf{z}}U_n(z; k) + i\hat{\mathbf{k}}V_n(z; k)]e^{i\mathbf{k}\cdot\mathbf{r}}, \qquad (3)$$

where z is height, $\hat{\mathbf{z}}$ is the unit vector pointing upward, and $\hat{\mathbf{k}}$ is the horizontal unit vector pointing in the direction of $\mathbf{k}$. Zero height corresponds to the photosphere ($-z$ is depth). The representation of the displacement eigenfunctions in terms of only the two functions U and V is possible as neither the f nor the p modes have horizontal motions that are perpendicular to $\mathbf{k}$.
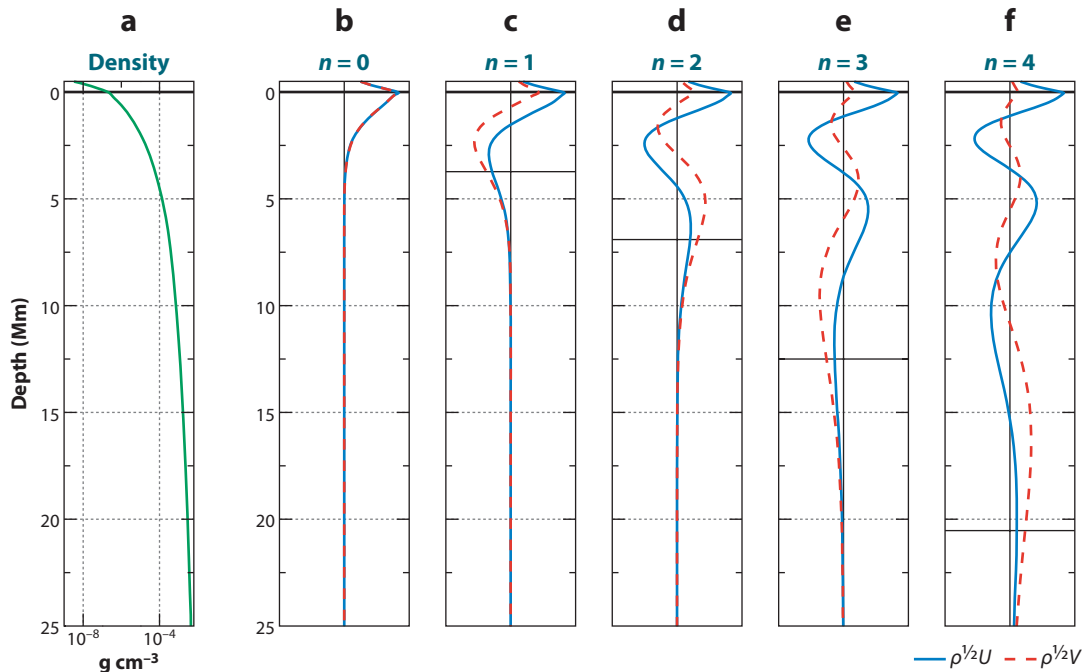
Figure 4

(*a*) Density profile from Model S (*green line*) and (*b-f*) mode eigenfunctions U and V for the radials order $n = 0$–4 at the frequency 3.5 mHz. The lower turning points of the modes $n = 1$–4 are shown as thin horizontal black lines. At fixed frequency, the horizontal phase speed ωk^{-1} increases with increasing radial order n, and therefore lower turning points increase with increasing n as well. The functions U and V have been scaled with $\rho^{1/2}$ as the kinetic energy density is proportional to $\rho(U^2 + V^2)$.

As a result of the assumed isotropy, the functions U and V do not depend on the direction of $\mathbf{k}$, and the mode frequencies $\omega_n(k)$ only depend on wave number. The time evolution of the mode $(n, \mathbf{k})$ is given by $\exp[-i\omega_n(k)t]$. In models that include attenuation, the frequencies are complex, though they are real for the case of adiabatic oscillations and standard boundary conditions.

Figure 4 shows the horizontal and vertical eigenfunctions corresponding to the first five radial orders at a frequency of 3.5 mHz. The solar model for this case is a plane-parallel version of Model S. The eigenfunctions are scaled by $\rho^{1/2}$, where ρ is the density (see **Figure 4a**). This scaling is used as we are interested in the kinetic energy density of the modes, $\rho(U^2 + V^2)$, which is a physically relevant quantity. For the f mode, the horizontal and vertical displacement eigenfunctions are equal. For the acoustic modes ($n > 0$), the lower turning point, z_t, is the height at which the sound speed is equal to the horizontal phase speed of the mode: $c(z_t) = \omega/k$ (neglecting the buoyancy frequency and the acoustic cutoff frequency, both of which are very small below a few megameters beneath the photosphere). Thus all the modes with a similar horizontal phase speed (a *straight line* through the origin in **Figure 3**) have a similar lower turning point and probe essentially the same layers of the Sun.

3. LOCAL HELIOSEISMOLOGY

This section overviews the various methods of local helioseismology. For an in-depth description of each method see, e.g., Gizon & Birch (2005) and references therein.

3.1. Ring-Diagram Analysis

The first operation in ring-diagram analysis is to cover some fraction of the visible solar disk with patches (overlapping or not) with circular areas with diameters in the range of 2°–30°. Each patch is tracked in longitude with a velocity close to the solar surface rotation velocity to produce a time series of helioseismic observations (Dopplergrams or intensity images). For each patch a 3D local power spectrum of the solar oscillation, P, is computed according to Equations 1 and 2. The local power spectra reflect the local physical conditions in the solar interior, such as wave speed and horizontal flows (Hill 1988). For example, a constant horizontal flow $\mathbf{u}$ will introduce a Doppler shift of the power spectrum:

$$P(\mathbf{k}, \omega) = P_0(\mathbf{k}, \omega - \mathbf{k} \cdot \mathbf{u}), \tag{4}$$

where P_0 is the power spectrum in the absence of a flow. This description is highly simplified as flows in the Sun do vary with horizontal position and depth. A change in the structure of the solar interior produces a change in the dispersion relation that does not depend on the direction of $\mathbf{k}$, and thus a change in the power spectrum that is also independent of the direction of $\mathbf{k}$.

There are two ways to study local power spectra. The first approach is to consider cuts at constant frequency, ω. In (k_x, k_y) space, wave power is concentrated in rings, each corresponding to a different radial order n (Hill 1988). A ring diagram is shown in **Figure 5**. When there is no flow, the radius of each ring is the wave number k at which $\omega_n(k) = \omega$ and is sensitive to the local dispersion relation. Thus, the ring radius is related to the local wave speed under the patch. As shown above, a flow will affect the local power spectrum. Linearizing Equation 4 for small $\mathbf{k} \cdot \mathbf{u}$, we find that the change in the ring position is $\delta \mathbf{k} = -(k/v_g)\mathbf{u}$, where $v_g = \partial_k \omega_n$ is the group speed. Hence, the flow amplitude and direction can be estimated from the orientation and distortion of the rings. Note that the distortion of a ring depends on radial order in the case of a depth-varying flow.
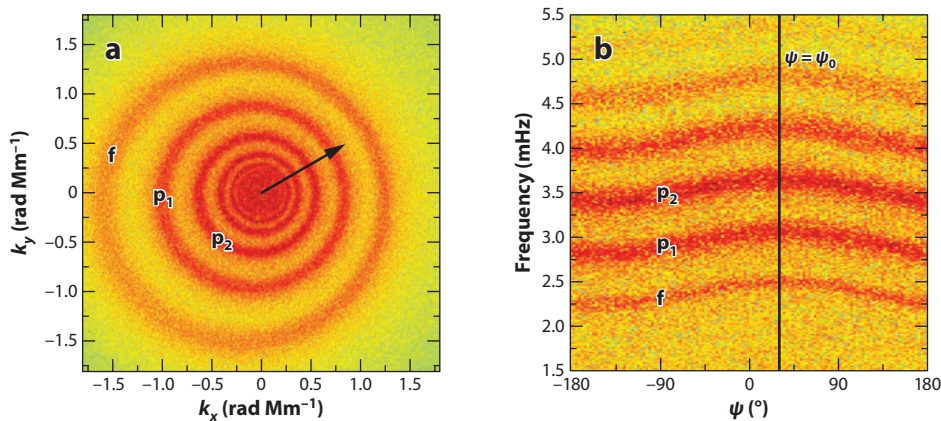

Figure 5

Slices through a model local power spectrum (*a*) at constant frequency $\omega/2\pi = 3.1$ mHz and (*b*) at constant wave number $k = 0.8$ rad Mm^{-1} for the case of a depth-independent horizontal flow $\mathbf{u}$ with an amplitude of 1 km s^{-1} and in the direction ψ_0 that is 30° north of the prograde direction. In panel *a*, the black arrow shows the direction of the flow. The different rings correspond to different radial orders; the outermost ring is the f mode. The rings with large k are more strongly influenced by the flow than those with small k. In panel *b*, the ridge frequencies show a sinusoidal variation with ψ and reach their maxima when $\psi = \psi_0$ (shown by the *vertical black line*). The frequency variation with ψ is the same for all of the ridges as the flow is independent of depth.

The second approach consists of considering cuts at constant wave number, k, through the power spectra (Schou & Bogart 1998). The local power spectra are then studied in (ψ, ω) space, where ψ is the azimuth of the wave vector measured from the prograde direction, $\hat{\mathbf{x}}$. The modes appear as bands of power around the resonant frequencies $\omega_n(k)$. According to Equation 4, a constant horizontal flow will Doppler shift the mode frequencies by $\delta\omega = \mathbf{k}\cdot\mathbf{u} = ku_x \cos\psi + ku_y \sin\psi$. As a result, $\mathbf{u}$ can be estimated from the frequency shifts at each k and radial order n. A change in the wave speed will simply manifest itself as a change in the wave frequencies that is independent of ψ and can be disentangled from the effect of a horizontal flow.

Both approaches rely on fitting a parametric model of the power spectrum to the observed local power spectra. Several functional forms have been proposed to fit the observations. The most important fitted parameters are the mode frequencies, $\bar{\omega}(n, k)$, and the two flow parameters, $\bar{u}_x(n, k)$ and $\bar{u}_y(n, k)$. There is one set of parameters for each wave number and radial order. Details about the fitting procedures are given by, e.g., Basu, Antia & Tripathy (1999) for the first approach and, e.g., Haber et al. (2000) for the second approach.

The fitted parameters are sensitive to the conditions in the solar interior, with a depth sensitivity that depends on the eigenfunction of the mode (e.g., Christensen-Dalsgaard 2002). For example, the depth sensitivity to a horizontal flow is approximately given by the kinetic energy density of the mode (e.g., Birch et al. 2007). The larger the horizontal phase speed of the mode, the deeper the sensitivity. Thus, large patches give access to deeper regions in the Sun than small patches. The differences between the fitted mode frequencies, $\bar{\omega}$, and the mode frequencies calculated from a standard solar model, $\omega_n(k)$, are used in 1D (depth) inversions to infer structural conditions under each patch (e.g., Basu, Antia & Bogart 2004). Two independent structural quantities can be inverted at a time, e.g., sound speed and density, from which other quantities can be inferred, such as the first adiabatic exponent. Similarly, the depth dependency of the horizontal flows, u_x and u_y, can be inferred from a set of fitted parameters $\bar{u}_x$ and $\bar{u}_y$ (Hill 1989). Typically, ring analysis is used to probe the top 30 Mm of the convection zone, with a maximum horizontal resolution of about 2° near the surface. Three-dimensional maps can then be obtained by combining neighboring patches.

3.2. The Cross-Covariance Function

Time-distance helioseismology is based on the measurement of the cross-covariance between the Doppler signals at two points $\mathbf{r}_1$ and $\mathbf{r}_2$ on the solar surface,

$$C(\mathbf{r}_1, \mathbf{r}_2, t) = \int_0^T dt' \, \phi(\mathbf{r}_1, t')\phi(\mathbf{r}_2, t' + t), \qquad (5)$$

where t is the correlation time lag. **Figure 6a** shows a cross-covariance function measured from 144 days of MDI medium-degree data. The cross-covariance has been averaged over many pairs of points $(\mathbf{r}_2, \mathbf{r}_1)$ and is presented as a function of the heliocentric angle between these two points. This diagram is known as the time-distance diagram. The cross-covariance is essentially a phase coherent average of the random oscillations (Bogdan 1997, and **Supplemental Video 2**). It is a solar seismogram: it provides a way to measure wave travel times between two surface locations.

A particular wavepacket (consisting of a set of modes with similar phase speeds) is preferentially selected for each travel distance. Many applications involve much less temporal and spatial averaging than was used in this Figure. Typical cross-covariances are therefore much noisier than the example shown here. The deeper meaning of the cross-covariance was elucidated only recently in terms of Green's functions (see sidebar, Extracting Information from a Random Wave Field).

An important tool for visualizing wave propagation in the Sun is the ray approximation (e.g., Kosovichev & Duvall 1997). In this approximation, the wavelength is treated as if it were much
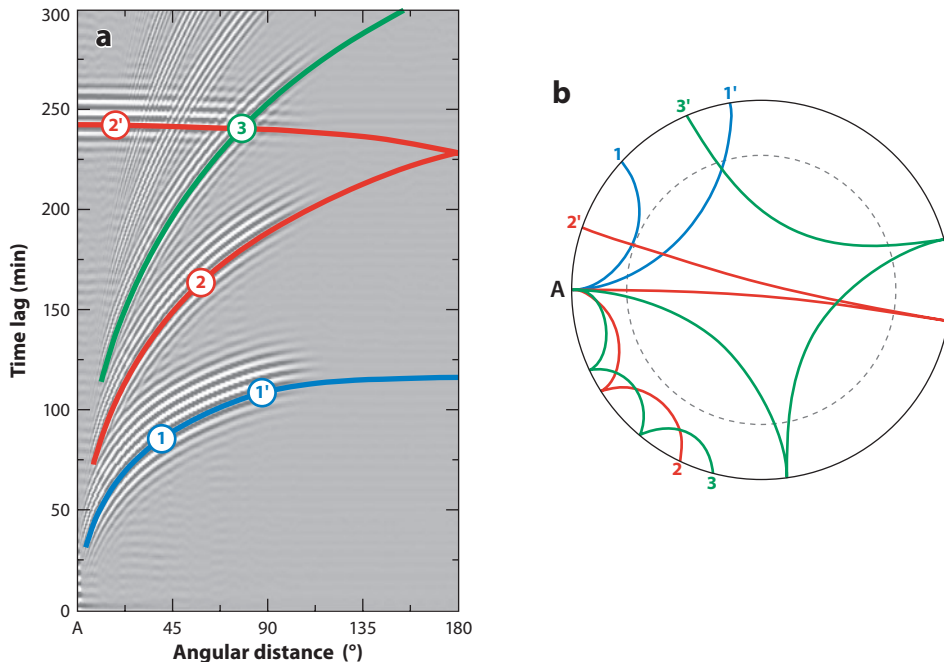
Figure 6

(*a*) Measured cross-covariance function for *Solar and Heliospheric Observatory*/Michelson Doppler Imager medium-degree data as a function of separation distance and time lag (Kosovichev, Duvall & Scherrer 2000). Positive values are white; negative values are black. The observation duration is $T = 144$ days starting in May 1996. (*b*) Example ray paths for acoustic wavepackets. In both *a* and *b*, the blue lines correspond to single-skip ray paths, the red lines are for two-skip ray paths, and the green lines are for three-skip ray paths.

EXTRACTING INFORMATION FROM A RANDOM WAVE FIELD

Duvall et al. (1993) first used the cross-covariance function to measure the travel time of wave packets between two locations on the solar surface. The cross-covariance averages the information over an ensemble of random waves, constructively. The concept of time-distance helioseismology has found many applications in physics, geophysics, and ocean acoustics (see reviews by Larose et al. 2006, Gouédard et al. 2008). Various experiments and observations (e.g., Weaver & Lobkis 2001, Shapiro et al. 2005) have shown that the cross-covariance is intimately connected to the Green's function, G, i.e., the response of the medium to an impulsive source. Recently, Colin de Verdière (2006) proved that in an arbitrarily complex medium containing a homogeneous distribution of white noise sources (standard deviation σ), the cross-covariance is given by

$$\frac{\partial}{\partial t} C(\mathbf{r}_1, \mathbf{r}_2, t) = -\frac{\sigma^2}{4\gamma} \left[G(\mathbf{r}_1, \mathbf{r}_2, t) - G(\mathbf{r}_1, \mathbf{r}_2, -t) \right],$$

when the integration time tends to infinity and the coefficient of attenuation (γ) tends to zero. In the Fourier domain, this is equivalent to saying that C is proportional to the imaginary part of the Green's function, Im $G(\mathbf{r}_1, \mathbf{r}_2, \omega)$. Although the above assumptions are too restrictive to be applied to the solar case, it is clear that the cross-covariance is a very important diagnostic to probe media permeated by random fields (wave fields or diffuse fields).

smaller than the length scales associated with the variations in the background solar model. The ray paths describe the propagation of wave energy and are analogous to the rays in geometrical optics. For discussions of the range of validity of the ray approximation see, e.g., Hung, Dahlen & Nolet (2000) and Birch et al. (2001).

Figure 6b shows some example ray paths computed from Model S. In this Figure, the rays all begin from the same point at the solar surface. Downward propagating rays are refracted by the increase of the sound speed with depth until they reach their lower turning point where the horizontal phase speed matches the sound speed. At frequencies below about 5.3 mHz, upward propagating rays are reflected from the solar surface by the sharp rise in the acoustic cutoff frequency. At higher frequencies, the waves escape into the solar atmosphere.

The main features in the time-distance diagram (**Figure 6a**) are the ridges, which correspond to different paths that wave energy takes between pairs of observation points. For example, the blue line corresponds to "first-bounce" arrivals (i.e., waves that visit their lower turning points once between the two observation points). The fine structure of the ridges in the time-difference diagram reflects the band-limited nature of the power spectrum. The majority of the wave power is near 3 mHz and, as a result, the cross-covariance shows fine structure that has a period of about 5 min. The other ridges seen in the time-distance diagram correspond to multiple bounces. One particularly important ray path is the third bounce ray path (**Figure 6b**, *green 3′*), which travels to the farside of the Sun before returning to the visible disk. This ray path plays a central role in farside imaging (Section 9). As can be seen in the example ray paths in **Figure 6b**, the depth of the lower turning point increases with the distance the ray travels in a single skip.

We note that the cross-covariance is directly related to the local power spectrum in the case when the medium is assumed to be horizontally invariant over this local area. In this case, the cross-covariance is simply given by the inverse Fourier transform of the local power spectrum (Gizon & Birch 2002):

$$C(\mathbf{r}_1, \mathbf{r}_2, t) = \text{const.} \int d^2\mathbf{k} \int d\omega \, P(\mathbf{k}, \omega) e^{i\mathbf{k}\cdot(\mathbf{r}_2 - \mathbf{r}_1) - i\omega t}. \tag{6}$$

Changes in the local power spectrum, such as those discussed above in the context of ring-diagram analysis, will affect the cross-covariance.

3.3. Time-Distance Helioseismology

Time-distance helioseismology (Duvall et al. 1993, 1997; Kosovichev 1996) consists of (*a*) measuring wave travel times from the cross-covariance function, and (*b*) inverting the travel times to infer the solar subsurface structure and flows.

As discussed in the sidebar (Extracting Information from a Random Wave Field), the cross-covariance $C(\mathbf{r}_1, \mathbf{r}_2, t)$ is closely related to a Green's function that gives the wave response at $(\mathbf{r}_2, t)$ to a source located at $(\mathbf{r}_1, t = 0)$. Thus, the cross-covariance is sensitive to the wave propagation conditions (structure and flows) between the two surface points $\mathbf{r}_1$ and $\mathbf{r}_2$. The sensitivity of the cross-covariance to any particular local change in the solar interior is a nontrivial research topic, because the local wavelength of solar oscillations is not necessarily small compared to the length scales of the heterogeneities in the Sun. In addition, this sensitivity depends strongly on the combination of waves that contribute to the cross-covariance function. This is discussed in Section 4.

For the sake of simplicity, consider a constant horizontal flow **u**. According to Equations 4 and 6, the effect of such a flow is a Galilean translation of the unperturbed (no flow) cross-covariance,

C_0, according to:

$$C(\mathbf{r}_1, \mathbf{r}_2, t) = C_0(\mathbf{r}_1, \mathbf{r}_2 - \mathbf{u}t, t). \tag{7}$$

In practice, this result is only an approximation because the power spectrum is often subject to additional filtering, which is not included in Equation 6 (Gizon & Birch 2002). The waves travel faster along the flow than against the flow. If $\mathbf{u}$ is directed from $\mathbf{r}_1$ to $\mathbf{r}_2$, then the $t > 0$ ridges of the time-distance diagram are shifted to smaller time lags t and the $t < 0$ ridges are shifted to more negative t. Thus, a flow breaks the symmetry between the $t > 0$ and $t < 0$ parts of the cross-covariance. In contrast, a horizontally uniform change in, e.g., sound speed would introduce a time-symmetric change in the cross-covariance.

Several techniques have been proposed to measure travel times from the cross-covariance. The (phase) travel times for inward- and outward-going waves are measured by fitting a Gabor wavelet to the two branches of the cross-covariance (Duvall et al. 1997, Kosovichev & Duvall 1997). The travel times can also be measured with a simple one-parameter fit (Gizon & Birch 2002, 2004), as is done in geophysics (e.g., Marquering, Dahlen & Nolet 1999).

The cross-covariance function computed between two spatial points is in general very noisy. Spatial averaging is a useful tool to reduce random noise. Duvall et al. (1997) considered an averaging scheme whereby the cross-covariance is computed between a point and a concentric annulus or quadrants of arc. For example, the cross-covariance between a point and an annulus is used to study waves that propagate outward from the central point to the annulus (positive time lag) and from the annulus inward to the central point (negative time lag). The difference between inward and outward travel times is sensitive to the horizontal divergence of the local flow or to a local vertical flow, while the average travel time is sensitive to the local wave speed. Similarly, the covariance between a point and a north quadrant is used to study waves that propagate either northward or southward. The various combinations of travel times are shown in **Figure 7** for annulus radii ranging from 12 Mm to 27 Mm. Each travel-time map is obtained by translating the central point of the annulus. With only a few hours of averaging, the travel-times differences are clearly sensitive to the supergranulation flows.

Finally, the travel-time maps must be inverted (the inverse problem). This requires a model for the relationship between the travel-time perturbations and perturbations in solar properties (the forward problem). Recent progress regarding the interpretation of travel time is described in Section 4.

3.4. Helioseismic Holography

Helioseismic holography (Lindsey & Braun 1997) and acoustic imaging (Chang et al. 1997), which are virtually indistinguishable, are closely related to the time-distance method. In both of these methods, observations of the wave field (e.g., Doppler velocity) at the solar surface are used to estimate the wave field in the solar interior. Separate estimates are constructed by computationally evolving the observed wave field either forward or backward in time. In helioseismic holography, these two estimates are called the ingression (H_-, propagates forward in time) and egression (H_+, propagates backward in time) and are computed as

$$H_{\pm}(\mathbf{r}, z, \omega) = \int_{\mathcal{P}} \mathrm{d}^2\mathbf{r}' \, G_{\pm}(||\mathbf{r}' - \mathbf{r}||, z, \omega)\phi(\mathbf{r}', \omega), \tag{8}$$

where $\mathbf{r}$ is the horizontal focus position, z is the focus depth, and the integration over surface positions $\mathbf{r}'$ is carried out over the region described by the "pupil" $\mathcal{P}$. The functions $G_{\pm}$ are causal (subscript $-$) and anticausal (subscript $+$) Green's functions. These Green's functions can
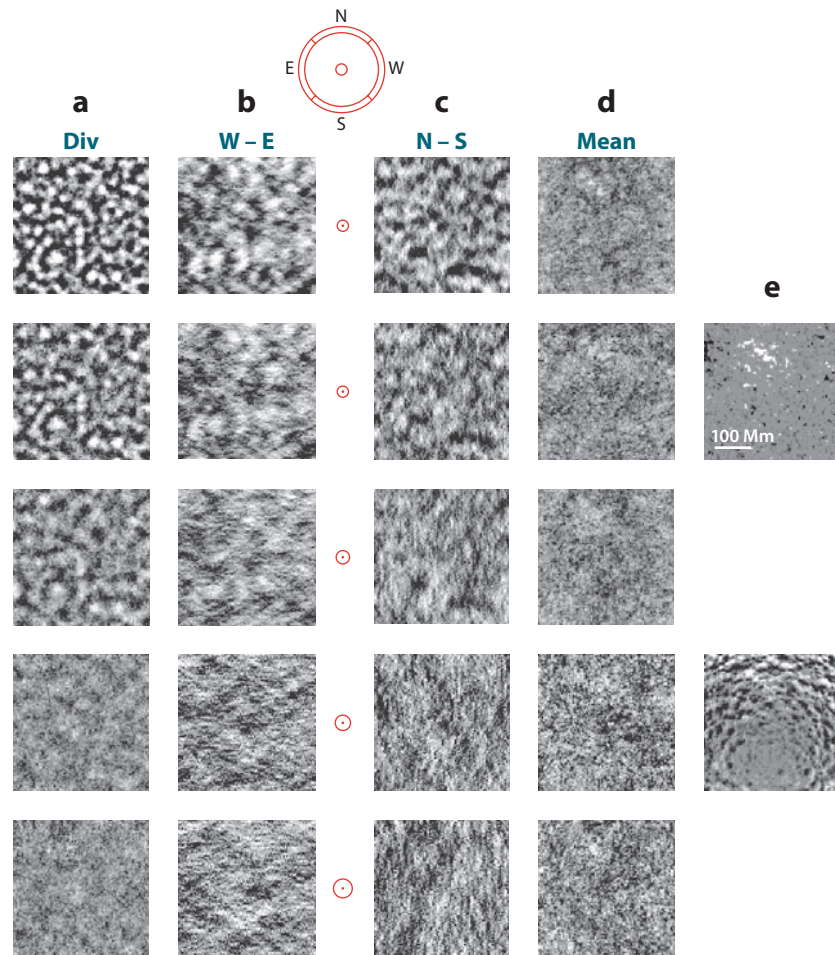
Figure 7

Maps of the travel times using the annulus/quadrant geometry and *Solar and Heliospheric Observatory/*
Michelson Doppler Imager high-resolution data (Duvall et al. 1997). The observation duration is $T =$
8.5 hr. Each frame is 370 Mm on a side. Each row corresponds to a different annulus radius from 12 Mm to
27 Mm. The columns show the four types of travel-time measurements: (*a*) travel-time difference between
the outward-going waves and the inward-going waves, (*b*) travel-time difference between the westward- and
eastward-going waves, (*c*) travel-time difference between the northward- and southward-going waves, and
(*d*) mean of the travel times of the inward- and outward-going waves. (*e, upper*) The average magnetogram
and (*e, lower*) the average Dopplergram. The travel-time perturbations are mostly due to the supergranular-
scale horizontal flows.

be thought of as propagators that (approximately) evolve the wave field either forward or backward
in time.

The amplitude and phase of the correlation between the two estimates $H_\pm$ contain information
regarding wave propagation in the Sun (e.g., Lindsey & Braun 1997, 2000). For example, in farside
imaging (Section 9), the phase of the ingression-egression correlation is used to detect active
regions.

3.5. Direct Modeling

Direct modeling (Woodard 2002, 2007) is a method for interpreting correlations in the wave field. These correlations, however, are not measured in real space but in the Fourier domain. For example, any steady heterogeneity in the Sun is expected to introduce correlations between incoming and scattered waves with different wave vectors but with the same frequency. Unlike time-distance helioseismology, direct modeling can also treat time-varying perturbations, which couple waves with different frequencies. One of the main characteristics of direct modeling, as its name suggests, is that it does not produce any intermediate data products (e.g., no travel-time maps) as the inversions are carried out directly on the correlations.

3.6. Fourier-Hankel Analysis

Fourier-Hankel analysis (Braun, Duvall & Labonte 1987) was specifically designed to study the wave field around sunspots. The analysis is carried out in a cylindrical coordinate system with origin centered on the sunspot. The wave field observed in an annular region around the sunspot is decomposed into inward and outward propagating components, using a Fourier-Hankel transform. The amplitudes and the phases of the incoming and outgoing waves can be compared in order to characterize the interaction of the waves with the sunspot. In particular, Fourier-Hankel analysis was the first method to measure the absorption coefficient of incoming waves by a sunspot (Braun, Duvall & Labonte 1987), defined by $(P_{in} - P_{out})/P_{in}$, where P_{in} and P_{out} are, respectively, the incoming and outgoing powers. In addition, the Fourier-Hankel method has been used to measure the phase shift between the incoming and outgoing waves, as well as the scattering from one mode to another (Braun 1995).

4. THE FORWARD AND INVERSE PROBLEMS

4.1. Weak Perturbation Approximation

Many important solar features can be reasonably approximated, in the context of wave propagation, as small deviations from a horizontally uniform reference model. Examples include the supergranulation, meridional flow, torsional oscillations, and subsurface (but not surface) magnetic fields. For this class of solar features, linear forward modeling can be employed. The main advantage of linear forward models is that they lead to linear inverse problems, which is the only class of inverse problems that can be solved easily.

4.1.1. Sensitivity functions. In linear forward models, the helioseismic measurements (e.g., travel-time shifts) can be related to weak, steady perturbations to a reference model through sensitivity functions (also called kernels) by equations of the form

$$d_i = \sum_\alpha \int_\odot K_i^\alpha(\mathbf{x}) \delta q_\alpha(\mathbf{x}) d^3\mathbf{x}, \qquad (9)$$

where the d_i stands for an arbitrary set of helioseismic measurements (for example, travel-time perturbations $\delta\tau_i$), the functions δq_α describe the deviations from the reference solar model, and the functions K_i^α are the corresponding kernel functions. The sum over α is over all types of perturbations to the solar model. A complete set of q_α includes, e.g., pressure, density, sound speed (c), flow velocity ($\mathbf{u}$), and magnetic field vector ($\mathbf{B}$). The integration variable $\mathbf{x}$ is a 3D position vector and runs over the entire reference solar model.

4.1.2. The ray approximation.

The ray approximation, in which the wavelength is approximated as small compared to the other length scales in the problem (e.g., the scale heights of the reference model, and the length scales of the perturbations δq^{α}) has been used extensively in time-distance helioseismology (e.g., Kosovichev 1996, Kosovichev & Duvall 1997) to compute the travel-time sensitivity functions K. A ray sensitivity kernel for the travel-time perturbation $\delta\tau(\mathbf{r}_1, \mathbf{r}_2)$ is zero everywhere except along the ray, Γ, that goes from $\mathbf{r}_1$ to $\mathbf{r}_2$ (see Section 3.2).

The starting point is the local dispersion relation

$$(\omega - \mathbf{k}_t \cdot \mathbf{u})^2 = c^2 k_t^2 + \omega_{ac}^2, \tag{10}$$

where ω is the angular frequency, $\mathbf{k}_t$ is the 3D total wave vector, $\mathbf{u}$ is the vector flow, c is the sound speed, and ω_{ac} is the acoustic cutoff frequency. In the ray approximation the travel time is given by the path integral of the phase slowness vector $\mathbf{k}_t/\omega$. Under the assumption that ω is constant, the travel time perturbation is given by

$$\delta\tau = \frac{1}{\omega} \int_{\Gamma} \delta\mathbf{k}_t \cdot \hat{\mathbf{n}} \, ds, \tag{11}$$

where $\hat{\mathbf{n}}$ is the unit vector along Γ and $\delta\mathbf{k}_t$ is the perturbation to the total wave vector caused by the flow $\mathbf{u}$, the change in the sound speed, δc, and the change in the acoustic cutoff frequency, $\delta\omega_{ac}$. Notice that the ray path, Γ, is assumed to be unchanged to first order. Although the ray approximation has played an important role in local helioseismology, it does not account for finite wavelength effects and other complications (cf. Birch et al. 2009, Bogdan 1997).

4.1.3. The first Born approximation.

In the first-order Born approximation, the perturbations δq_α cause a perturbation to the wave field that is due to single scattering only. In this approximation, first-order finite wavelength effects, such as Fresnel zones and wave front healing, are included (e.g., Hung, Dahlen & Nolet 2001). The Born approximation has been used in the seismology of the Earth (e.g., in the search for mantle plumes by Montelli et al. 2004). Gizon & Birch (2002) give a detailed theoretical treatment of the application of the Born approximation to problems in time-distance helioseismology.

Born kernels for the effects of sound-speed changes on travel times have been obtained by, e.g., Birch & Kosovichev (2000) and Jensen, Jacobsen & Christensen-Dalsgaard (2000). Born kernels for flows have been computed for time-distance helioseismology by Gizon, Duvall & Larsen (2000), Birch et al. (2007), and Jackiewicz et al. (2007). Three-dimensional sensitivity kernels for flows and ring-diagram analysis are given by Birch & Gizon (2007). Although magnetic perturbations are expected to be small just a few hundred kilometers below the surface (Gizon, Hanasoge & Birch 2006), corresponding kernels have not been obtained yet.

Figure 8 shows slices through an example travel-time sensitivity kernel for perturbations in the squared sound-speed ($\delta d_i = \delta\tau$ and $q_\alpha = c^2$ in Equation 9). The main features are that the kernel is zero along the ray path, is maximum (absolute value) in a shell around the ray path, and shows substantial ringing. These kernels have been called banana-doughnut kernels in the context of seismology of the Earth (Marquering, Dahlen & Nolet 1999). The zero along the ray path is owing to the lack of a geometrical delay (change in path length) for small scatterers located on the reference ray path. In the solar case, there are additional hyperbolic features across the ray path, owing to the presence of distant sources (Gizon & Birch 2002).

The first-order Born approximation has been tested using exact solutions (e.g., Gizon, Hanasoge & Birch 2006) and numerical simulations (e.g., Hung, Dahlen & Nolet 2000; Birch et al. 2001; Baig, Dahlen & Hung 2003; Birch & Felder 2004) for simple cases. Duvall, Birch & Gizon
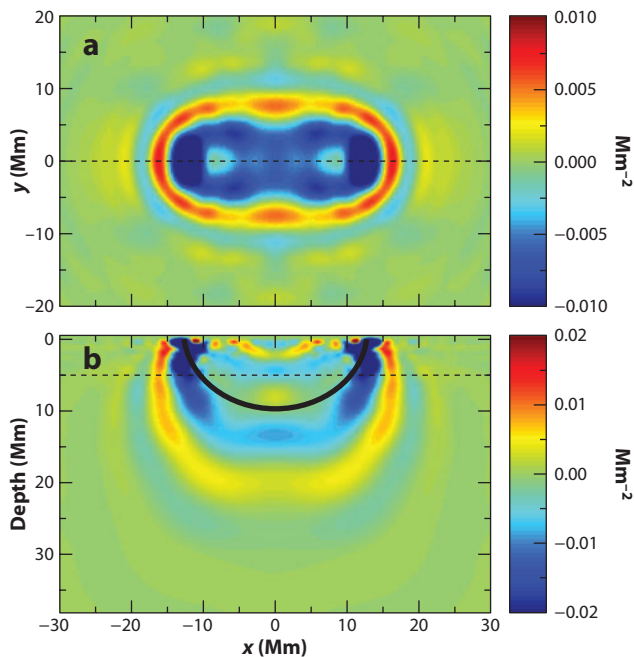
Figure 8

Linear sensitivity of a single-skip mean travel-time shift to local changes in the square of the sound speed. The observation points are located at $(x, y, z) = (\pm 12.5, 0, -0.2)$ Mm. (*a*) A horizontal slice at a depth of 5 Mm. (*b*) A vertical slice at $y = 0$; the heavy black line shows the single-skip ray path connecting the observation points. The kernel has been scaled with the background sound speed to enhance the visibility of the subsurface structure. The ringing away from the ray path is due to the band-limited nature of solar oscillations. The linear sensitivity is almost zero along the ray path; this is a generic feature of sound-speed kernels in three dimensions and is well known in seismology (Dahlen, Hung & Nolet 2000; Marquering, Dahlen & Nolet 1999).

(2006) used solar observations to construct 2D travel-time kernels using small (subwavelength) magnetic features as point scatterers.

4.1.4. Inversions and resolution kernels. Linear inversions have been developed for ring-diagram analysis and time-distance helioseismology, based on experience gained from global helioseismology (e.g., Christensen-Dalsgaard, Schou & Thompson 1990 and references therein). Two different inversion procedures are commonly used.

Let us consider 1D depth inversions for the sake of simplicity. The first inversion method, called regularized least squares (RLS, e.g., Kosovichev 1996, Haber et al. 2000), is simply a fit to the observational data δd_i under conditions of smoothness. The second inversion method, called optimally localized averaging (OLA, Haber et al. 2004), looks for a linear combination of the kernels (an averaging kernel) that is spatially localized around a target depth, $-z_0$. Both methods build averaging kernels of the form

$$\mathcal{K}(z; z_0) = \sum_i c_i(z_0) K_i^\alpha(z), \qquad (12)$$

where the c_i are coefficients to be determined. A regularization is applied to ensure that the error on the inferred q_α is not too large or that q_α is smooth. In addition, the cross talk between the inferred q_α and all other quantities q_β, $\beta \neq \alpha$, should be avoided. Inversions require a good knowledge of

Figure 9

Averaging kernels from 1D regularized least squares inversions for ring-diagram analysis (depth sensitivity to horizontal flows). The numbers (in units of megameters) refer to the average depths of the averaging kernels. Courtesy of Irene González-Hernández.
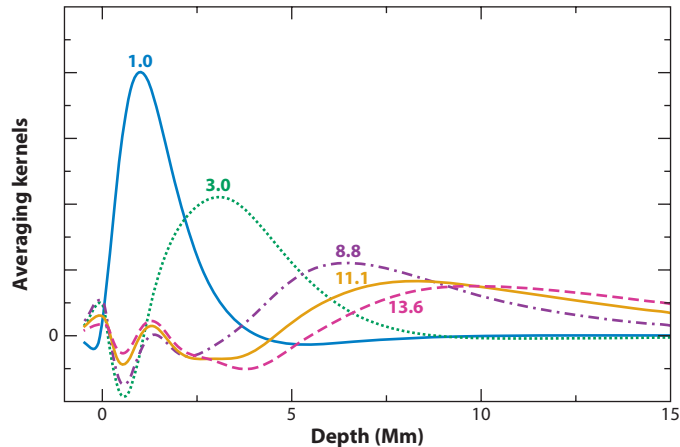
the noise covariance matrix of the measurements, which can be estimated directly from the data (spatial averaging) or from a model (Gizon & Birch 2004).

The RLS and OLA methods give similar answers, although the RLS averaging kernels are perhaps more likely to have undesired sidelobes near the surface (Haber et al. 2004). **Figure 9** shows example RLS averaging kernels for ring-diagram analysis in the near-surface layers. These particular kernels are used to infer horizontal flows. Very similar averaging kernels are obtained for time-distance helioseismology (e.g., Jackiewicz, Gizon & Birch 2008).

Most time-distance inversions assume that the kernels are invariant by horizontal translation, so that the horizontal convolution of the kernels with the δq_α becomes a multiplication in Fourier space. This property is used to speed up the inversions (Jacobsen et al. 1999).

Recent progress includes the inclusion of the Born kernels in the inversions and the noise correlations (e.g., Couvidat et al. 2005). An OLA inversion for the horizontal and vertical components of the flows was implemented by Jackiewicz, Gizon & Birch (2008), in which the Born kernels and the noise covariance matrix are both consistent with the definition of the observed travel times. We note that the vertical component of velocity has been indirectly estimated from ring-diagram inversion by requiring mass conservation (e.g., Komm et al. 2004).

4.2. Strong Perturbation Regime

The solar atmosphere is permeated by concentrations of magnetic field with strength $B > 1$ kG. This magnetic field profoundly affects the solar atmosphere as well as the solar oscillations in the upper layers (Bogdan & Cally 1995 and references therein). The effects on the waves are not small and it is formally not justified to employ a single-scattering approximation to describe them. For example, the first Born approximation is not expected to capture the interaction of f and p modes with the near-surface layers of sunspots (e.g., Gizon, Hanasoge & Birch 2006).

The Lorentz force is an additional restoring force that permits the existence of new oscillation modes. In the case of a spatially uniform model with no gravity, it is possible to identify three types of magnetohydrodynamics (MHD) waves: the fast, slow, and Alfvén waves. In gravitationally stratified magnetized atmospheres, this classification can only be applied locally. The waves couple near the layer where the sound speed and the Alfvén speed, $a = B/\sqrt{4\pi\rho}$, are equal (e.g., Schunker & Cally 2006). In a typical sunspot, the $a = c$ surface is only a few hundred kilometers below the quiet-Sun photosphere.

RLS: regularized least squares

OLA: optimally localized averaging (or averages)

Quiet Sun: regions with low levels of magnetic activity, away from active regions

The ray approximation can be extended in order to study wave propagation in MHD problems (e.g., Schunker & Cally 2006). The magnetic field affects travel times, mode frequencies, and amplitudes. These effects depend sensitively on the geometry, in particular the angle between the incident wave vector and the magnetic field vector at the $a = c$ layer. **Figure 10** shows two example ray calculations for the case of an incoming acoustic wave approaching the solar surface from below (the magnetic field, wave vector, and gravity are in the same plane). In these two calculations, all of the parameters are the same except that the angle of the magnetic field has been changed. In **Figure 10** (*top*), the wave vector of the acoustic wave is nearly aligned with the magnetic field at the $a = c$ layer.
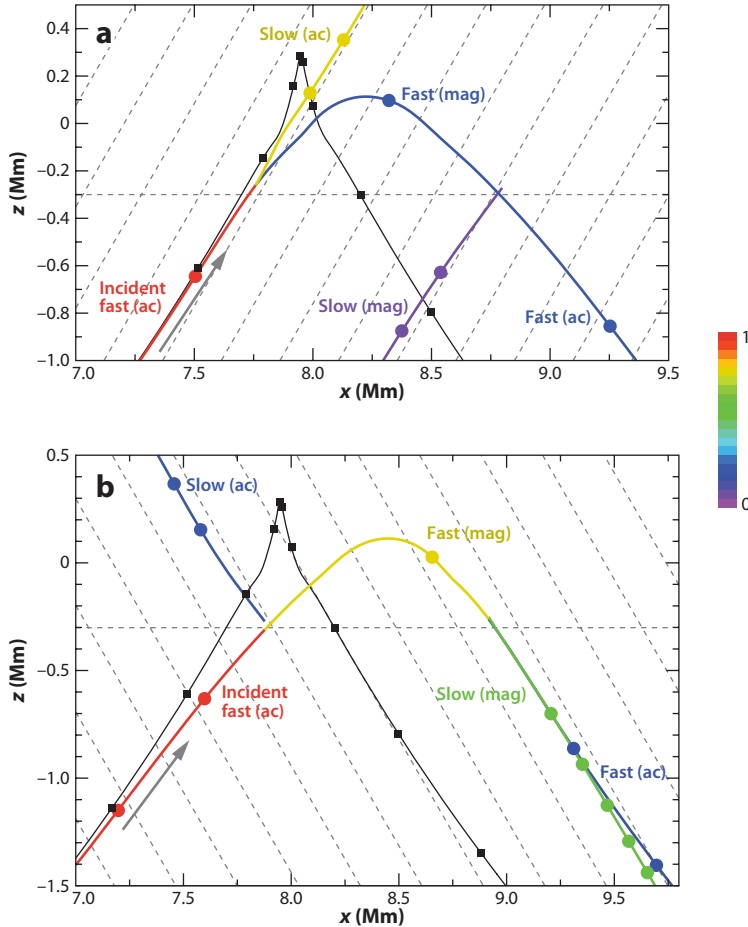
Figure 10

Ray paths in model surface layers with 2 kG uniform magnetic field inclined at $\pm30°$, respectively, to the vertical, as shown by the background gray lines. The incoming 5-mHz rays (*gray arrows*) have lower turning points at $z = -5$ Mm and are shown in red. The two frames correspond to two different attack angles. The horizontal gray line indicates where the sound speed and the Alfvén speed coincide, which is approximately where mode conversion happens. The fractional energy remaining in each resulting ray is indicated by the color legend. The dots on the ray paths indicate 1-min group travel-time intervals. The thin black curve represents the acoustic ray that would be there in the absence of magnetic field. Note that the fast ray is faster through the surface layers than the nonmagnetic ray. Figure and caption from Cally (2007). Figure copyright *Wiley-VCH Verlag GmbH & Co. KGaA*. Reproduced with permission.

In this case, most of the energy is transmitted to the acoustic (slow) mode of the $a > c$ region. This acoustic mode escapes along the magnetic field lines (ramp effect). Some energy is, however, converted to the fast (magnetic) mode, which is then refracted by the increase of the Alfvén speed with height. In **Figure 10** (*bottom*), the incident wave vector makes a large angle with the magnetic field. At the $a = c$ level, the acoustic wave converts mostly into a magnetic (fast) mode that is refracted back into the Sun and then mostly becomes a downward propagating magnetic (slow) mode, while a small fraction of energy continues in a fast mode. The slow mode is not seen again at the surface, and thus removes energy from the surface wave field. **Supplemental Videos 3–6** illustrate generalized ray theory for various values of the attack angle between the wave vector and the magnetic field. We note that in three dimensions, where the magnetic field, wave vector, and gravity are not all coplanar, strong coupling to the Aflvén wave also occurs (Cally & Goossens 2008).

Numerical simulations are an important tool to study waves in magnetized regions and sunspots. Two different approaches are employed. The first approach is numerical simulations of wave propagation through prescribed background models (e.g., Cally & Bogdan 1997; Khomenko & Collados 2006; Cameron, Gizon & Daiffallah 2007; Hanasoge 2008; Parchevsky & Kosovichev 2009). This approach permits the study of wave propagation without the complications of solving for convection and it gives the freedom to choose various background models. Typically, these codes solve the equations of motion for small-amplitude waves. The second approach is realistic numerical simulations of magnetoconvection (e.g., Rempel et al. 2009). Such simulations include self-excited waves and aim at simulating realistic solar active regions. This approach is very promising, but computer intensive.

Figure 11 shows an example calculation of the propagation of a p_1 wave packet through a simple sunspot model using the 3D code of Cameron, Gizon & Daiffallah (2007). This example shows that the transmitted wave packet is phase-shifted by the sunspot (increased effective wave speed) and has a reduced amplitude compared to the quiet-Sun value. Also seen is the partial conversion of incoming p modes into downgoing slow modes. This process is responsible for absorption of acoustic energy by sunspots (Spruit & Bogdan 1992, Cally & Bogdan 1997, Crouch & Cally 2005, and Section 6). An f mode wave packet is affected in a similar fashion (Cally & Bogdan 1997; Cameron, Gizon & Duvall 2008).

The problem of inferring the subsurface structure and dynamics of solar active regions is a difficult one. In principle, standard linear inversions cannot be used because surface magnetic perturbations are not small with respect to a quiet-Sun reference model. No nonlinear inversion has been implemented yet. Instead there have been attempts to construct simple parametric models of magnetic regions, which have a helioseismic signature that is consistent with the observations. This approach does not require that perturbations be small. Forward models of sunspots have been proposed by, e.g., Crouch et al. (2005) and Cameron, Gizon & Duvall (2008); they are discussed in more detail in Section 6.4.

Now that we have some understanding of the methods of local helioseismology and their diagnostic potential, we turn to a description of the main observational results: near-surface convection (Section 5), sunspots (Section 6), extended flows around active regions (Section 7), global scales (Section 8), farside imaging (Section 9), and flare-excited waves (Section 10).

5. NEAR-SURFACE CONVECTION

5.1. Supergranulation and Magnetic Network

Solar supergranules are horizontal outflows with a typical size of 30 Mm, outlined by the chromospheric network (e.g., Leighton, Noyes & Simon 1962). They have horizontal velocities of order 200 m s^{-1} and lifetimes of one to two days.
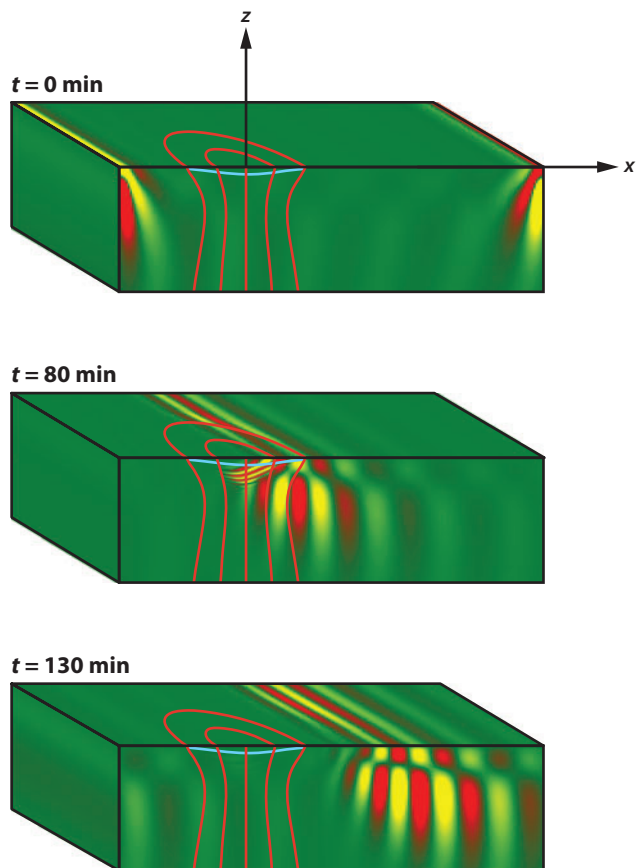
Figure 11

Numerical simulation of the propagation of a p_1 plane wavepacket through a model sunspot using the magnetohydrodynamic code of Cameron, Gizon & Daiffallah (2007). The sunspot model is a magnetic semiempirical model (Cameron et al. 2010) with a maximum vertical field $B_z = 3$ kG at the surface; it is embedded in a Model S background atmosphere stabilized with respect to convection. The wavepacket is initially located 43.7 Mm to the left of the sunspot and propagates to the right. The x-component of velocity is shown at times $t = 0$, 80, and 130 min (positive values in *red*, negative values in *yellow*). The $a = c$ level is represented by the blue curve. The dimensions of the displayed domain are -43.7 Mm $< x < 102.0$ Mm, $0 < y < 36.4$ Mm, and -20 Mm $< z < 1.5$ Mm in all panels. Only half ($y > 0$) of the computational domain is shown. The boundary conditions are periodic in the horizontal directions and there are two sponge layers (not shown here) at the top and at the bottom of the box to avoid the reflection of the waves back into the computational domain. The $t = 80$ min snapshot clearly shows the slow magneto-acoustic-gravity waves propagating down the sunspot. Because these slow waves are transverse, they are easily seen as oscillations in the x-component of velocity. See **Supplemental Video 7**.

Duvall et al. (1997) found that p-mode travel times contain information at supergranular length scales (**Figure 7**). As a demonstration of this, the line-of-sight component of velocity, estimated from the travel times assuming that vertical motions are negligible, was found to be highly correlated with the time-averaged Dopplergram, thus confirming that local helioseismology is capable of probing convective flows at supergranulation length scales. Duvall & Gizon (2000) extended the analysis to f modes to infer horizontal flows within 2 Mm below the surface. Because they propagate horizontally, f modes are well suited to measure horizontal flows and their horizontal

divergence. The flows from f-mode time-distance helioseismology compare well with flows estimated from local correlation tracking of mesogranulation (De Rosa, Duvall & Toomre 2000). Recently, Woodard (2009) has shown that direct modeling can be used to detect convection on scales of space and time that are smaller than those of supergranulation.

Figure 12 shows the most recent inversion of travel times (Jackiewicz, Gizon & Birch 2008) using modes f through p_4. This inversion incorporates a full treatment of finite-wavelength effects
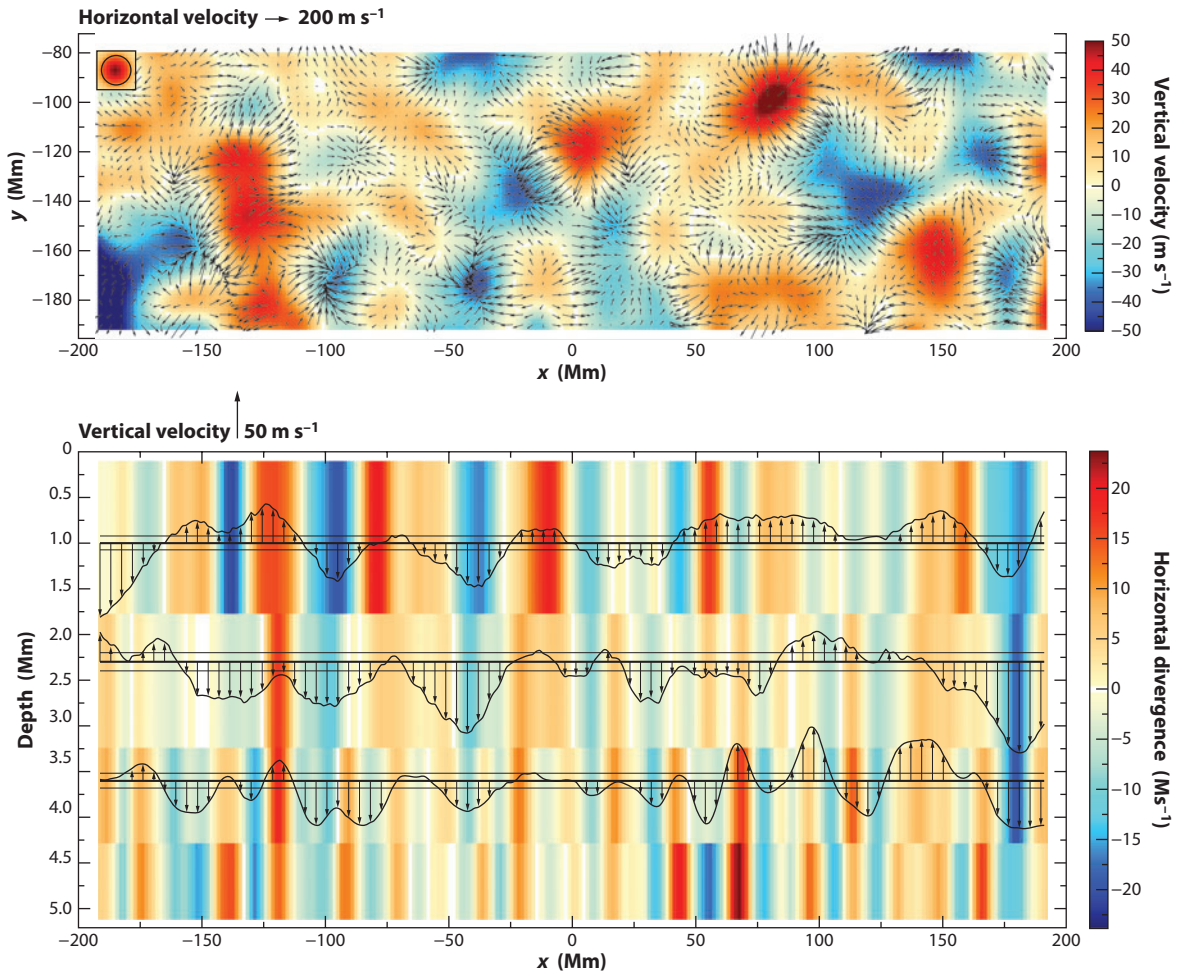
Figure 12

Inversion for vector flows in the near surface layers. The travel times were measured for ridges f and p_1 through p_4 and inverted using an optimally localized averaging technique. The observation time is $T = 3$ days. (*top*) Horizontal slice at the depth of 1 Mm showing the two horizontal components (u_x and u_y, *arrows*) and the vertical component (u_z, *colors*) of the vector flow field. The FWHM of the averaging kernel is 10 Mm (*inset in top-left corner*). The most visible features correspond to long-lived supergranules. (*bottom*) Vertical slice at $y = -176$ Mm (*white line in top panel*) showing the horizontal divergence of the flow field as a function of x and depth (*colors*) from the same 2+1D inversion. The vertical arrows show the vertical velocity u_z for the three ridges f, p_1, and p_2 (from *top* to *bottom*) from a 2D horizontal inversion, plotted at the depths corresponding to the mean depth of the respective averaging kernels. The one-sigma level of random noise in u_z is equal to 10 m s^{-1} by construction (*horizontal black lines*). Adapted from Jackiewicz, Gizon & Birch (2008).

(first-order Born approximation), modeling of the details of the measurement procedure, and a treatment of the statistical properties of noise. The vector flow field, averaged over $T = 3$ days, is dominated by long-lived supergranules. As seen in the Figure, the divergent flows are cospatial with upflows, with about 20 m s^{-1} rms velocity (with maximum values of $\sim$50 m s^{-1}). Near the surface, the vertical velocity can be measured with a noise level as low as 10 m s^{-1} for 24 hours of data and a horizontal resolution of about 10 Mm. Estimates of the vertical velocity in supergranules from direct Doppler measurements can only be obtained near disk center and are in the range 10–30 m s^{-1} (Hathaway et al. 2002 and references therein), which is consistent with the results of local helioseismology.

Because noise reduction requires time averaging, the finite lifetime of supergranulation implies a strict limitation on the maximum depth at which we can probe the flow field before it evolves substantially. Using the f and p_1–p_4 modes, Woodard (2007) found that random noise dominates below about 4 Mm. Probing supergranules at greater depth involves statistical analysis over large fields of view and many supergranulation lifetimes in order to reduce the noise: this allows the study of the average properties of the flows at depth. Inversions of convective flows tens of megameters below the surface are challenging as they require excellent models of the sensitivity of travel times to subsurface flows (see Braun & Lindsey 2003, for a discussion) and claims of the detection of a supergranulation return flow are apparently inconsistent (e.g., Duvall 1998, Zhao & Kosovichev 2003).

The pattern of divergent flows in the surface layers is outlined by a network of small magnetic features (see Duvall & Gizon 2000, Braun & Lindsey 2003, and **Supplemental Video 8**). This can be understood as the magnetic field is swept by the flows and concentrates at the boundaries of supergranules (e.g., Galloway, Proctor & Weiss 1977). The connections between the magnetic network and the propagation behavior of acoustic waves in the solar chromosphere can be studied by cross-correlating the observations of solar oscillations at multiple heights in the solar atmosphere (Finsterle et al. 2004b). Jefferies et al. (2006) showed that inclined magnetic field lines at the boundaries of supergranules provide "portals" through which low-frequency ($<$5 mHz) slow MAG waves can propagate up into the solar chromosphere (see **Figure 13**). This is because the cutoff frequency is lowered in the magnetic network relative to the quiet Sun by a factor of $\cos\theta$, where θ is the inclination of the magnetic field to the vertical. These low-frequency upward traveling waves have been suggested to act as a source of heating of the quiet-Sun chromosphere—as an alternative to Joule heating due to magnetic field reconnection or mechanical heating due to high-frequency waves.

▶ Supplemental Material

5.2. Rotation-Induced Vorticity

Rotation is expected to have a small effect on the dynamics of the supergranulation through the Coriolis force. As solar convection is highly turbulent, this effect can only be studied in a statistical sense using several months of data. For example, in the northern hemisphere, divergent flows are expected to have a slight positive correlation with clockwise vertical vorticity. Duvall & Gizon (2000) and Gizon & Duvall (2003) used time-distance helioseismology to make the first measurement of this small effect. After removing the average rotation and meridional circulation from the inferred flows, Gizon & Duvall (2003) studied the relationship between the horizontal divergence of the flows, denoted by div, and the vertical component of vorticity, denoted by curl. **Figure 14a** shows the latitudinal dependency of $\langle curl\rangle_+$ and $\langle curl\rangle_-$, respectively, defined as the averages of the curl over regions of positive and negative div. In the northern hemisphere, diverging flows preferentially rotate clockwise, whereas converging flows preferentially rotate counter-clockwise. This pattern is reversed in the southern hemisphere. This situation is an expected consequence of the Coriolis force. Furthermore, the latitudinal dependency of $\langle curl\rangle_+$ and $\langle curl\rangle_-$ is observed to

Mean SOHO/MDI B$_{//}$

MOTH Na-K phase travel-time
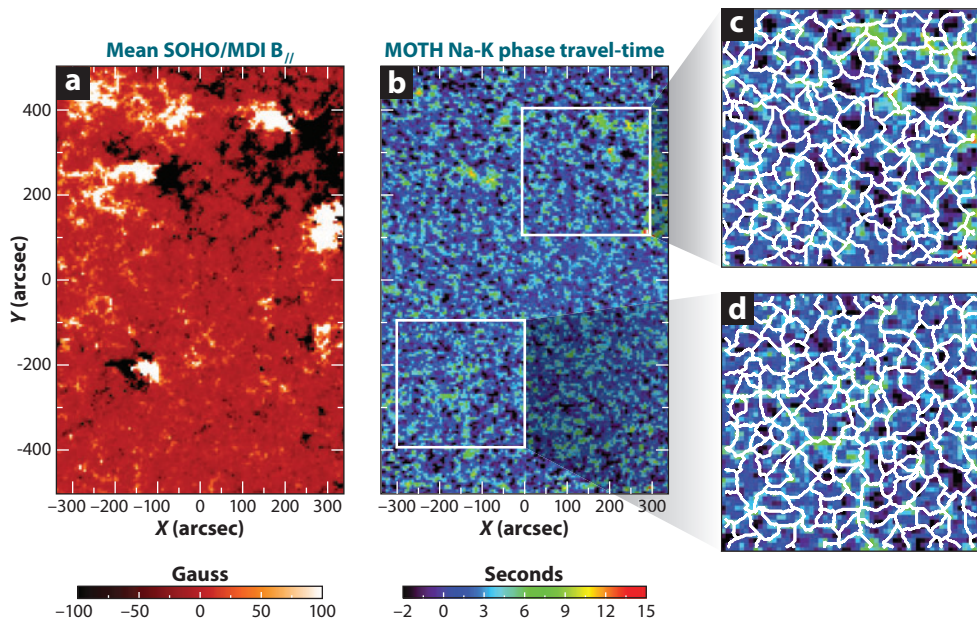
Gauss

Seconds

Figure 13

(*a*) Map of the average *Solar and Heliospheric Observatory*/Michelson Doppler Imager line-of-sight component of the magnetic field in the Sun's photosphere for the 107-hr period starting 06:59 UT on January 6, 2003. (*b*) Map of phase travel time Finsterle et al. (2004b) for magneto-acoustic-gravity waves with frequencies near 3 mHz based on contemporaneous, simultaneous Doppler velocity data as viewed at 5,890 Å (Na) and 7,699 Å (K). (*c,d*) Magnified views of two regions of the phase-travel-time map overlaid with an estimate of the location of the boundaries of the supergranular-scale convective cells as determined using a segmentation of the mean intensity image at 5,890 Å. Note that there is not a significant travel-time signal in all of the observed plages, only in regions where the field is highly inclined. This signal is noticeably larger than that in the boundaries of the supergranules. This is probably due to the larger magnetic filling factor in the plage. Figure and caption from Jefferies et al. (2006).

be nearly exactly proportional to the radial component of the solar angular velocity, $\sin(\lambda)\Omega(\lambda)$, where λ is latitude and Ω is the solar angular velocity.

Observations (**Figure 14*b***) show that the horizontal average of the product of div by curl is given by

$$\langle \text{div curl} \rangle \simeq -3 \times 10^{-10} \sin(\lambda)\Omega(\lambda)/\Omega_{eq}\ s^{-2}, \tag{13}$$

where Ω_{eq} is the equatorial angular velocity. Simple dimensional analysis of the equations of motion predicts that $\langle \text{div curl} \rangle \sim -\text{Co}(\lambda)/\tau^2$, where $\text{Co}(\lambda) = 2\tau\Omega(\lambda)\sin(\lambda)$ is the local Coriolis number and τ is the characteristic correlation time of the turbulence. For example, $\tau = 2$ days implies $\text{Co}(\lambda)/\tau^2 \sim 3 \times 10^{-11} \sin(\lambda)\Omega(\lambda)/\Omega_{eq}\ s^{-2}$. It is not clear if this difference of a factor of ten indicates missing physics or simply reflects the uncertainty in such estimates. Attempts at improved quantitative results suffer from arbitrarily tunable parameters.

Cyclonic convection is a means to generate poloidal field from toroidal field and is thus important in many dynamo models (for a recent review see Charbonneau 2005). In these models, the sign of the kinetic helicity $\mathcal{H}_{kin} = \langle \mathbf{u} \cdot (\nabla \wedge \mathbf{u}) \rangle$ determines the strength (and sign) of this effect. Helioseismic measurements imply that the kinetic helicity at supergranulation scales is negative in the northern hemisphere (and positive in the south). This is an estimate rather than a direct
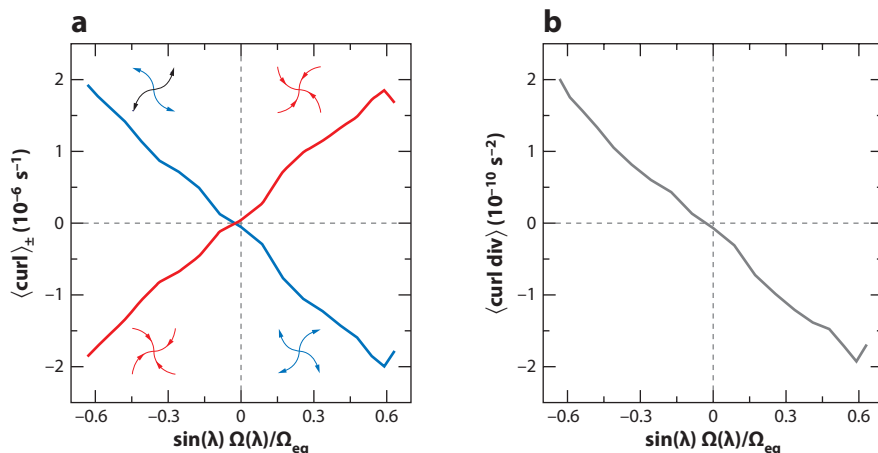
Figure 14

Effect of the Coriolis force on supergranulation flows. (*a*) Vertical vorticity (curl) averaged over regions with positive horizontal divergence ($\langle\text{curl}\rangle_+$, *blue curve*) and negative horizontal divergence ($\langle\text{curl}\rangle_-$, *red curve*) as functions of $\sin(\lambda)\Omega(\lambda)/\Omega_{eq}$, where λ is the heliographic latitude and Ω/Ω_{eq} is the local surface angular velocity relative to the equator. A vorticity of 10^{-6} s^{-1} corresponds to an angular velocity of 2.5° day^{-1} or a typical tangential velocity of 10 m s^{-1}. (*b*) Horizontal average $\langle\text{curl div}\rangle$ versus $\sin(\lambda)\Omega(\lambda)/\Omega_{eq}$. Adapted from Gizon & Duvall (2003).

measurement because the horizontal components of the vorticity have not yet been measured directly.

5.3. Evolution of Supergranulation Pattern

Gizon, Duvall & Schou (2003) studied the Fourier spectrum of long time series of maps of the horizontal divergence of the flows at supergranulation scales, measured using f-mode time-distance helioseismology. The observations reveal surprising characteristics: the signal has wavelike properties (period around 6 days), and power is anisotropic (excess power in the prograde and equatorward directions). These observations have been confirmed independently by Zhao (private communication) and Braun (private communication) using p-mode helioseismology. The power peaks at a nonzero frequency that increases slightly with horizontal wave number. Measurements of the Doppler shift of this apparent dispersion relation have provided a robust method for measuring the rotation and meridional flow of the solar plasma (Gizon, Duvall & Schou 2003, Gizon & Rempel 2008). An interesting aspect of this work is that the inferred rotation and the meridional flow match the motion of the small magnetic features (e.g., Komm, Howard & Harvey 1993a, 1993b). However, correlation tracking measurements applied to the divergence maps overestimate rotation and underestimate the meridional flow by large amounts (see Gizon & Birch 2005). The time evolution of the supergranulation pattern does not reflect its advection by the plasma flow, although the two can be decoupled in Fourier space.

We note that Hathaway, Williams & Cuntz (2006) demonstrated that the local correlation tracking of Doppler features on the Sun gives biased estimates of the rotation rate because of line-of-sight projection effects. This case, however, is not directly comparable to the observations described above, because helioseismic divergence maps are not expected to be sensitive to line-of-sight projection effects at supergranulation scales.

The helioseismic observations of the wave-like properties of supergranulation are still calling for an explanation. Supergranulation may perhaps be related to the traveling convection modes seen in idealized systems with rotation (e.g., Busse 2007).

6. SUNSPOTS

In this Section, we discuss the anchoring problem (Section 6.1), inferred flows in the immediate vicinity of sunspots (Section 6.2), the absorption of waves by sunspots (Section 6.3), and the subsurface structure of sunspots (Section 6.4). Recent reviews about sunspots are provided by, e.g., Solanki (2003) and Thomas & Weiss (2008). The absence of a sufficiently conclusive theory has allowed a wide range of ideas about the origin and structure of sunspots to develop. These range all the way from intuitive ideas directly inspired by the abundant observational clues to mathematically oriented ones that require ignoring almost all of these clues. Some of the ideas should become testable if they make relevant predictions for the relatively shallow layers below the surface that are accessible to local helioseismology methods.

6.1. The Anchoring Problem

The magnetic forces exerted by the spot on its surroundings are significant. If it were not in a quasi-stable equilibrium in its observable layers, a spot would evolve on the time for the Alfvén speed to cross the size of the spot (on the order of an hour), much shorter than the observed lifetimes of spots (days to weeks). The magnetic forces also make the sunspot plasma buoyant. Together, this gives rise to an anchoring problem (cf. Parker 1979). A sunspot cannot be just a surface phenomenon because magnetic field lines have no ends. The sunspot's field lines continue below the surface. In contrast with a scalar pressure field, the magnetic field of a sunspot cannot be kept in equilibrium simply by pressure balance at the surface: the tension in the magnetic field lines continuing below the surface exerts forces as well. The magnetic tension acting at the base of the spot keeps it together and prevents buoyancy from spreading it like an oil slick over the solar surface. Sunspots also rotate faster than the solar surface, indicating that they sense the increase of rotation with depth.

The question of sunspot equilibrium thus involves deeper layers, down to wherever the field lines continue. At which depth and by which agent is the sunspot flux bundle kept together? A very stable location is the boundary of the convection zone with the stably stratified radiative interior of the Sun. A layer of magnetic field floating on this boundary becomes unstable only at a field strength of about 10^5 G (Schüssler et al. 1994). The existence of such a critical field strength was hypothesized by Babcock (1961). The subsequent rise to the surface is what creates the observed bipolar active regions, as proposed by Cowling (1953). The action of the Coriolis force on flows in the magnetic field associated with the instability produces the poloidal field of the next cycle and is observable on the surface in the form of the systematic tilt of active region axes with respect to the azimuthal direction (Leighton 1969). A boost of confidence has been provided by recent realistic 3D radiative MHD simulations of the last stages of the emergence process of magnetic fields at the surface. These are beginning to look much like real observations (Cheung et al. 2008). Though largely qualitative, the view of the solar cycle developed by Babcock and Leighton appears to be the most fruitful frame of reference for interpreting the solar cycle.

6.2. Moat Flow

In the photosphere, sunspots are typically surrounded by diverging horizontal outflows, termed moat flows, with amplitudes of several hundred meters per second. These outflows typically extend
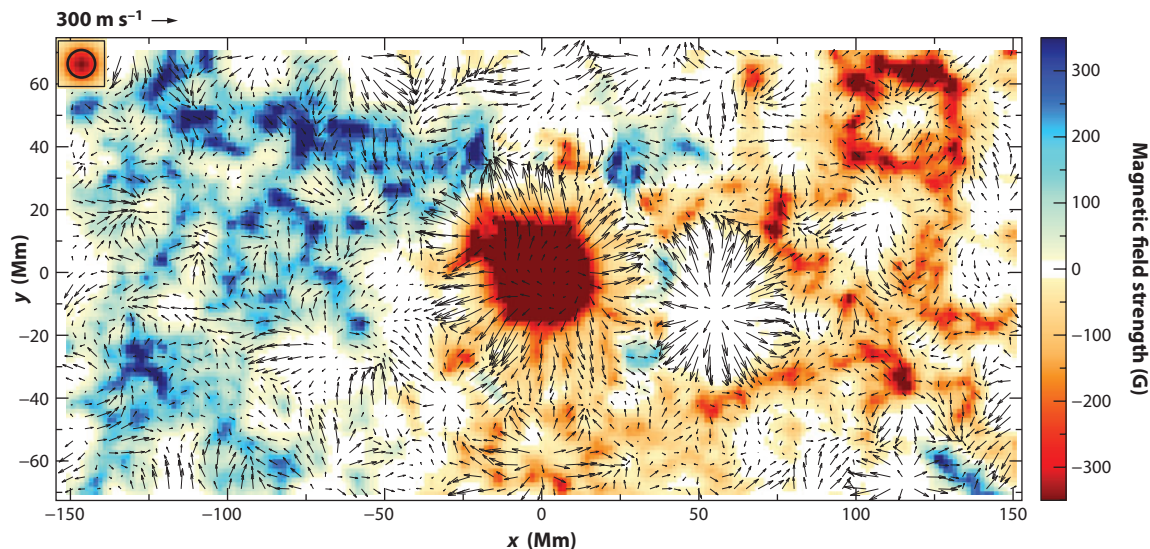
Figure 15

Moat flow around the sunspot in Active Region NOAA 9787 (see **Figure 2**) using the same time-distance inversion as in **Figure 12a**. The background colors show the *Solar and Heliospheric Observatory/*Michelson Doppler Imager line-of-sight component of the magnetic field. The depth is 1 Mm and the observation time is $T = 1$ day. The random noise in each horizontal component of the flow is estimated to be 17 m s^{-1}. Adapted from Gizon et al. (2009) by Jason Jackiewicz.

to about twice the radius of the penumbra. Moat flows were first detected using direct Doppler measurements (Sheeley 1972) and also can be inferred from the motion of small magnetic features (e.g., Brickhouse & Labonte 1988).

Local helioseismology is a useful tool for studying flows around sunspots (Duvall et al. 1996, Lindsey et al. 1996). Gizon, Duvall & Larsen (2000) used f-mode time-distance helioseismology to study the moat flows in the 2 Mm below the surface. Comparisons between the near-surface flows inferred from local helioseismology with direct Doppler measurements have demonstrated the validity of the near-surface inversions. **Figure 15** shows the moat flow at a depth of 1 Mm using a time-distance inversion and all ridges from f through p$_4$ (Gizon et al. 2009). At this depth, the moat flow has an amplitude of $\sim$250 m s^{-1}, which is consistent with the motion of the small magnetic features. This outflow is detected in the top 4 Mm. Such measurements of the subsurface moat flow have been confirmed by ring-diagram analysis.

The moat flow is believed to be driven by a pressure gradient caused by the blockage of heat transport by sunspots (e.g., Nye, Bruning & Labonte 1988). For a more accurate description in terms of the surface cooling that causes the observed flows, see Spruit (1997). Though much slower, the moat flow appears physically connected with the Evershed flow in the penumbra. This is evident both from the observations by, e.g., Cabrera Solana et al. (2006) and the realistic numerical simulations of Heinemann et al. (2007) and Rempel et al. (2009).

6.3. Absorption of Solar Oscillations

The first major discovery made by local helioseismology was that solar oscillations (f and p modes) are absorbed by sunspots (Braun, Duvall & Labonte 1987). This discovery was made using Fourier-Hankel analysis, which is based on the decomposition of the wave field around the sunspot into

ingoing and outgoing waves. Braun, Duvall & Labonte (1987, 1988) found that typical sunspots can absorb up to 50% of the incoming power.

Spruit & Bogdan (1992) proposed that mode conversion between the oscillations of the quiet Sun and the slow MAG waves of the sunspot could explain the observations of wave absorption by sunspots. Theoretical modeling (Cally & Bogdan 1993, Crouch et al. 2005) and numerical simulations (Cally 2000; Cally & Bogdan 1997; Cameron, Gizon & Duvall 2008) demonstrated that mode conversion is indeed capable of removing a large fraction of the energy from the helioseismic waves incident on a sunspot. The efficiency of the mode conversion is strongly dependent on the angle of the magnetic field from the vertical, with a maximum in the absorption occurring at an angle of about 30° from the vertical (Cally, Crouch & Braun 2003). Comparisons between observations and models (e.g., Cameron, Gizon & Duvall 2008; Crouch et al. 2005) show that the explanation of mode conversion is consistent with the observations of the reduction of outgoing wave power. We note that plage regions are also known to absorb incoming waves.

6.4. Phase Shifts and Wave-Speed Perturbations

Fourier-Hankel analysis (Section 3.6) has demonstrated that outgoing waves from sunspots have different phases than the corresponding ingoing waves (Braun et al. 1992, Braun 1995). At fixed radial order, the phase shifts increase roughly linearly with increasing angular degree. Fan, Braun & Chou (1995) used a simple model, in which the sunspot is treated as a local enhancement in the sound speed, to suggest that these phase shifts are indicative of a near-surface change in the wave speed relative to quiet Sun. Crouch et al. (2005) showed that approximate models of wave propagation in a model sunspot (embedded magnetic cylinders) could simultaneously explain the absorption and phase shift measurements. The success of these simple models suggests that the interaction of solar oscillations with the sunspot magnetic fields may be the essential physics in understanding both wave absorption (Section 6.3) and the phase shifts caused by sunspots.

Time-distance helioseismology, holography, and ring diagrams have all been used to infer changes in the wave speed in sunspots (e.g., Kosovichev 1996; Kosovichev, Duvall & Scherrer 2000; Jensen et al. 2001; Basu, Antia & Bogart 2004; Couvidat, Birch & Kosovichev 2006; among a great many others). Interpretation of the helioseismic measurements is a rapidly developing topic of current research. **Figure 16** shows a comparison between time-distance and ring-analysis inversions, forward models based on Fourier-Hankel analysis, and a realistic numerical simulation of a sunspot. As was shown by Gizon et al. (2009), there is not yet agreement among the different analysis methods, especially between the time-distance and ring-diagram results. There are a number of possible explanations for this disagreement. Current inversions for the time-distance and ring-diagram methods use sensitivity functions that do not explicitly include the direct effects of the magnetic field, and both assume that wave-speed perturbations are small. The time-distance sensitivity functions may not model the reference power spectrum sufficiently accurately (convective background, mode frequencies, relative mode amplitudes, line widths, and asymmetries). Neither method fully accounts for the details of the measurement procedures, especially in the case of time-distance, where the effects of the data analysis filtering in Fourier space (e.g., phase-speed filters) are not fully accounted for. Except for the time-distance inversion, all other methods are consistent with an increased wave speed in the top 2 Mm and show wave-speed perturbations with amplitudes less than about 2% at greater depths.

Direct simulation of wave propagation through sunspot models is useful to test the validity of these models. Cameron, Gizon & Duvall (2008) used a 3D MHD code to compute the propagation
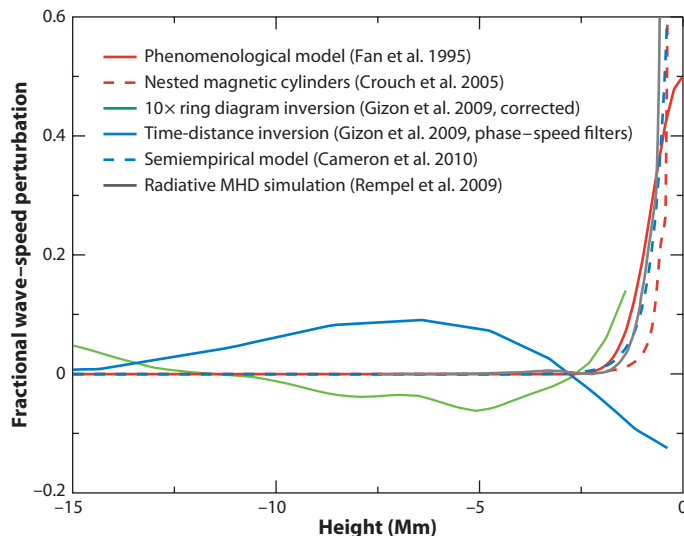
Figure 16

Fractional wave-speed perturbations under sunspots relative to quiet Sun. The perturbations are measured along sunspot axes except for the case of (unresolved) ring-diagram analysis. The solid red line shows a phenomenological model based on the Fourier-Hankel analysis of the sunspot in Active Region NOAA 5254 during November 27–30, 1988 (Fan, Braun & Chou 1995). The dashed red curve shows the fast wave speed, $c_f = (c^2 + a^2)^{1/2}$, in Active Region NOAA 5254 from the forward model of Crouch et al. (2005) that consists of nested magnetic cylinders. The green and solid blue lines give the wave-speed perturbations under the sunspot in Active Region NOAA 9787 (January 20–27, 2002) inferred from ring-diagram analysis and time-distance helioseismology using phase-speed filters (Gizon et al. 2009). The same tracked patch (diameter 15°) was analyzed in both cases. Because the sunspot is not spatially resolved in the ring analysis, a factor of ten is applied to facilitate the comparison. The two analyses give inconsistent estimates of the subsurface wave-speed perturbations. Possible explanations for this disagreement are described in the text. The dashed blue line is the fast wave speed of the semiempirical model of Cameron et al. (2010), based on the umbral model of Maltby et al. (1986) and used in the simulations of **Figures 11** and **17**. The black curve is the fast wave speed from the radiative magnetohydrodynamic (MHD) numerical simulation of Rempel et al. (2009).

of f modes through a model sunspot. Here we show a computation for the propagation of a p_1 wave packet using the same simulation code. The simulated wave field, which is the solution to an initial value problem, is compared to the observed cross-covariance in **Figure 17** in order to assess the validity of the underlying sunspot model. As for the f modes, the comparison with the observations is promising: The amplitude of the transmitted waves is reduced and the waves travel faster in the sunspot than in quiet Sun.

As mentioned in Section 4.2, sunspot magnetic fields strongly affect the nature of the wave properties in the surface layers. In particular, upward propagating high-frequency ($\omega > \omega_c$) waves are reflected and refracted at the $a = c$ surface, where MHD mode conversion occurs. Finsterle et al. (2004b) used multiheight observations of solar oscillations to map the $a = c$ surface in active regions, called the magnetic canopy. The travel time measured between two observation heights in the solar atmospheres was used to derive the propagation properties of the waves between these two layers. When both heights are above the $a = c$ layer, waves are evanescent and the travel time vanishes. Using combinations of three heights, they find that in sunspots and active regions the canopy dips below the base of the photosphere by several hundred kilometers, whereas it is above 1,000 km in the quiet Sun.
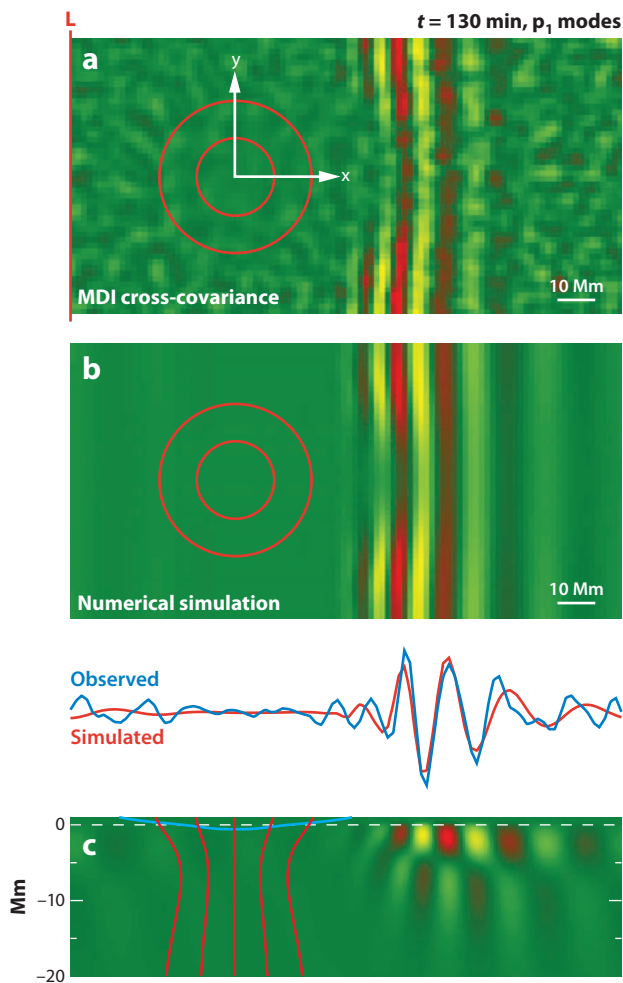
Figure 17

Sunspot time-distance helioseismology and forward numerical modeling. (*a*) The observed covariance, $C(\mathbf{r}, t) = \int dt' \bar{\phi}(t')\phi(\mathbf{r}, t' + t)$, between the *Solar and Heliospheric Observatory/*Michelson Doppler Imager (MDI) Doppler velocity averaged over the red line (*L*) at $x = -43.7$ Mm, $\bar{\phi}(t')$, and the Doppler velocity delayed by $t = 130$ min, $\phi(\mathbf{r}, t' + t)$. The horizontal coordinates $\mathbf{r} = (x, y)$ are centered on the sunspot. The color scale is such that positive values of C are red and negative values are yellow. The two red circles indicate the boundaries of the umbra and penumbra of the sunspot in Active Region NOAA 9787. The Doppler observations were filtered to select only the p_1 acoustic modes. To reduce noise, the cross-covariance was averaged over nine days (January 20–28, 2002) and over angles using the azimuthal symmetry of the sunspot. (*b*) Numerical simulation of wave propagation through the sunspot model of Cameron et al. (2010) as in **Figure 11**, except that here the vertical component of velocity, v_z, is shown. The initial conditions were chosen such that v_z matches the observed cross-covariance in the far field. The observed C and the simulated v_z are averaged over -2.5 Mm $< y < 2.5$ Mm and plotted as functions of x. For this particular model sunspot, the simulation provides a good match to the observed cross-covariance. (*c*) The simulated v_z in the *x*–*z* cut through the sunspot. The vertical scale is given in units of megameters and the $a = c$ level is shown by the blue curve. See **Supplemental Video 7**. A similar analysis was performed by Cameron, Gizon & Duvall (2008) for f-mode wave packets.

7. EXTENDED FLOWS AROUND ACTIVE REGIONS

In this section, we describe flows around large complexes of magnetic activity. These flows should not be confused with the (smaller scale) moat flow around individual sunspots discussed in Section 6.

7.1. Surface Inflows, Deeper Outflows

Using f-mode time-distance helioseismology, Gizon, Duvall & Larsen (2001) detected weak ~50-m-s^{-1} surface flows that converge toward active regions (**Figure 18**). These inflows, which exist as far as 30° from the centers of active regions, are also seen in ring-diagram analyses (e.g., Haber et al. 2001, 2004; Komm et al. 2007). In fact, Hindman et al. (2004) showed that the time-distance and ring-diagram methods give nearly identical results near the surface. The near-surface flows also agree reasonably well with the motion of supergranules (e.g., Švanda, Zhao & Kosovichev 2007). The converging flows near the surface are accompanied by cyclonic flows with vorticity of order 10^{-7} s^{-1} (Komm et al. 2007).

At depths in the range of about 10 Mm to 15 Mm, diverging flows from active regions have been inferred using the time-distance (Zhao & Kosovichev 2004) and ring-diagram (Haber et al. 2004) methods. These diverging flows typically have amplitudes of order 50 m s^{-1}. Komm et al. (2004) used ring-diagram measurements together with the constraint of mass conservation to infer downward flows of order 1 m s^{-1}, at depths less than about 10 Mm, in and around active regions. Below this depth, the active regions tend to show upflows.
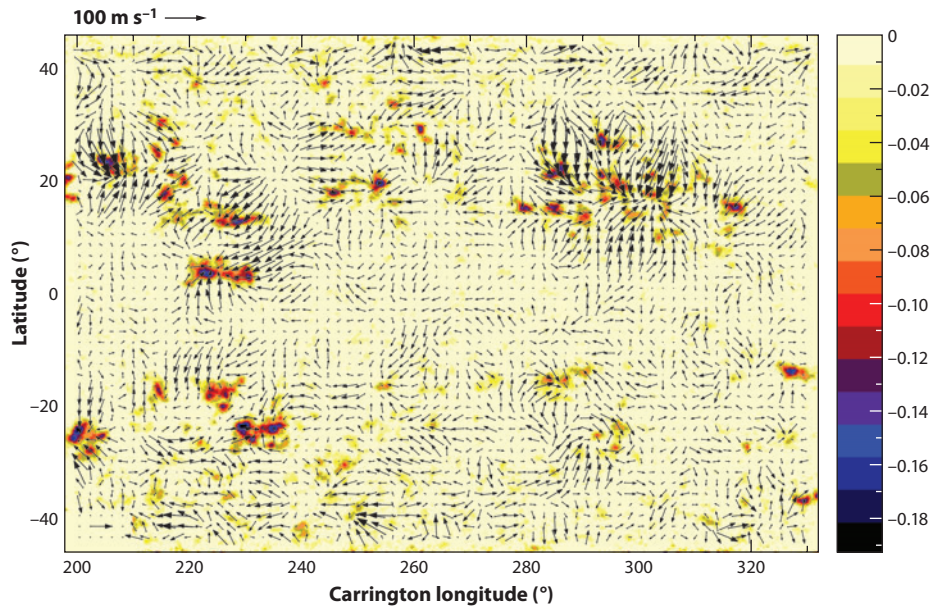

Figure 18

Synoptic map of local horizontal flows in the top 2 Mm below the solar surface, obtained with f-mode time-distance helioseismology. The horizontal and vertical axes give the longitude and the latitude in heliographic degrees. The data were averaged in time (7 days) in a frame of reference that corotates with the Sun (Carrington rotation rate). The flow maps were further processed to remove the average differential rotation and meridional flow. The color scale gives the fractional change in f-mode travel times with respect to quiet Sun: Reduced travel times correlate with magnetic activity. Adapted from Gizon, Duvall & Larsen (2001).
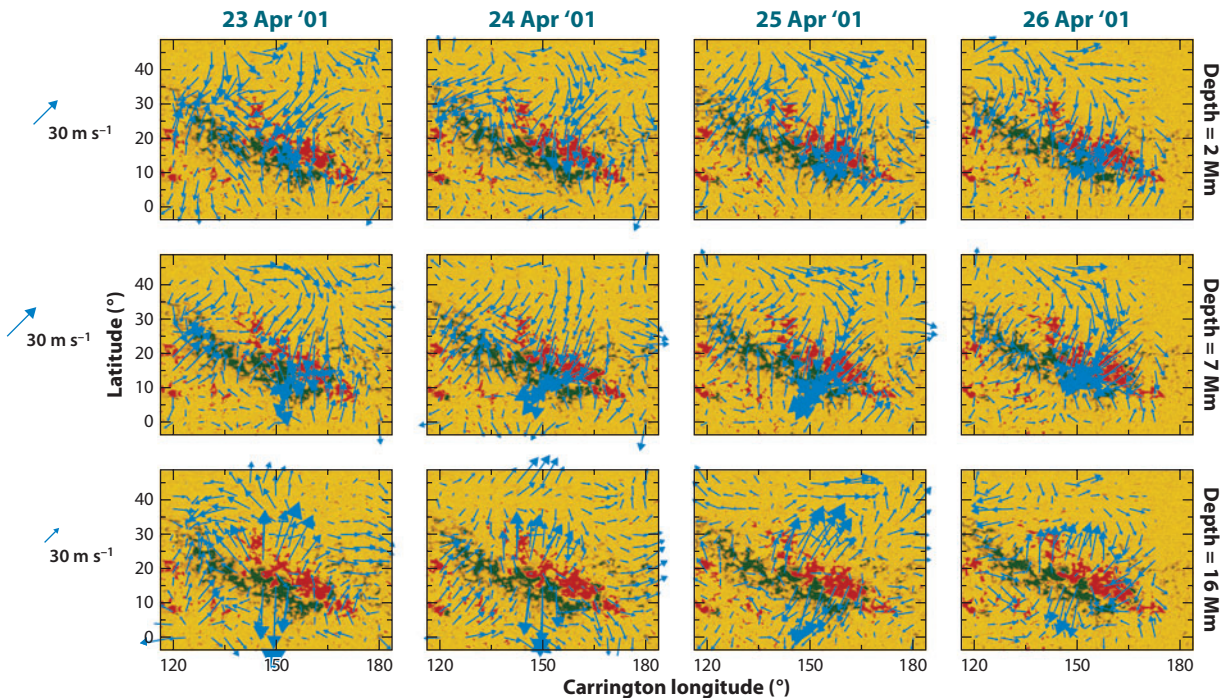
Figure 19

Daily averages of the horizontal flows around Active Region NOAA 9433 from April 23, 2001 until April 26, 2001 (one column for each day) inferred from ring-diagram analysis (Haber et al. 2004). The depths shown are 2 Mm (*top row*), 7 Mm (*middle row*), and 14 Mm (*bottom row*). The green and red shades are for the two polarities of the surface magnetic field (Michelson Doppler Imager magnetograms). The transition between inflow and outflow occurs near 10 Mm depth.

The observations are summarized in **Figure 19**, which shows the organization of horizontal flows around a particular complex of magnetic activity at three different depths. The flow patterns are consistent from day to day, despite the presence of supergranulation noise.

7.2. Flows Due to Thermal Effects of Magnetic Fields

A diagnostically important class of flows are those associated with thermal effects owing to magnetic fields, such as heating by dissipation of magnetic energy or the enhanced radiative loss of small-scale magnetic fields at the surface. On intermediate to large scales and timescales exceeding the rotation period, approximate geostrophic balance holds in the convection zone. Hence, flows of the thermal wind type must accompany thermal disturbances on those scales. For example, the enhanced radiative loss from the small-scale magnetic field in active regions has a cooling effect that should drive an inflow at the surface and a circulation, in the cyclonic sense, around the active region (Spruit 2003), as in low-pressure systems in the Earth's atmosphere. This may be an explanation for the flows described in the previous section.

8. GLOBAL SCALES

The dominant global-scale flows in the Sun are the differential rotation and the meridional flow. Helioseismic measurements made over long timescales (a few solar rotation periods) effectively

remove the contribution of small-scale convective flows and active region flows and allow high-precision studies of these global-scale flows. Both rotation and the meridional flow show small variations with the solar cycle.

8.1. Differential Rotation

The north-south symmetric component of internal differential rotation has been measured using global helioseismology (cf. review by Thompson et al. 2003). The solar rotation rate depends strongly on latitude in the convection zone; the equator rotates more quickly than the poles. The rotation rate shows only a weak radial shear in the bulk of the convection zone. There is strong radial shear in the very near-surface layers (top 35 Mm; Schou et al. 1998) and in the tachocline where the differentially rotating convection zone meets the uniformly rotating radiative zone. The tachocline plays an important role in most dynamo theories of the solar cycle.

As the differential rotation is well known, it provides an important test of local helioseismic methods. Giles, Duvall & Scherrer (1998) measured rotation with time-distance helioseismology applied to MDI data and found good qualitative agreement with the results of global helioseismology. Basu, Antia & Tripathy (1999) and González Hernández et al. (2006) both used ring-diagram analysis to study the differential rotation in the near-surface shear layer. These studies found rotation rates that essentially agreed with those inferred from global helioseismology in the top 20 Mm (increasing angular velocity with depth); below that depth the measurements showed instrument-dependent systematic errors.

8.2. Meridional Flow

Doppler measurements (e.g., Hathaway 1996) reveal a surface meridional flow with an amplitude of about 15 m s^{-1} from the equator to the poles. It has also been measured by tracking magnetic elements (Komm, Howard & Harvey 1993b), with essentially the same result. This surface meridional flow implies a subsurface return (i.e., equatorward) flow.

In flux-transport dynamo models (e.g., Dikpati & Charbonneau 1999, Charbonneau 2005), the meridional flow is responsible for the redistribution of flux from the active latitudes to the poles (at the surface) and, in some models, also from the poles to equator (at the base of the convection zone). Hathaway et al. (2003) argued that the equatorward drift of sunspots during the course of the solar cycle (the butterfly diagram) implies the existence of a 1.2 m s^{-1} return flow at the bottom of the convection zone. However, Schüssler & Schmitt (2004) argue that the butterfly diagram could be reproduced by a traditional model of dynamo waves without transport of magnetic flux by a flow.

In addition to its role in some dynamo theories, the meridional flow is also thought to play an important role in transporting angular momentum, and thus in maintaining the differential rotation (for a recent review see Miesch 2005).

The meridional flow produces a second-order shift in the frequencies of the global modes (unlike, for example, the differential rotation, which produces a first-order shift) and is therefore very difficult to measure using traditional global helioseismology. The meridional flow does, however, produce a first-order change in the eigenfunctions of the modes of the Sun, and thus produces first-order effects in local helioseismic measurements.

Giles et al. (1997) used time-distance helioseismology to obtain the first detection of the subsurface meridional flow. Imposing a mass conservation constraint, inversions of the time-distance measurements suggested a meridional flow that fills the convection zone, is equatorward below about 0.8 $R_\odot$, and has a strength of about 2 m s^{-1} at the base of the convection zone (Giles 2000). These deep results, however, are not direct measurements.

Figure 20 shows measurements of the meridional flow close to the surface using ring-diagram analysis and (a variant of) time-distance helioseismology. The maximum amplitude of the meridional flow is about 15 m s^{-1}. The eleven years of data show that the meridional flow varies significantly (up to 50% of its mean value). The solar-cycle dependency of the meridional flow is discussed in the next section.

As discussed by Braun & Birch (2008), one of the fundamental difficulties in measuring the deep meridional flow is that the noise level, owing to the stochastic nature of solar oscillations, is very large compared to the weak signal expected from a flow of a few meters per second (for comparison, the sound speed at the base of the convection zone is roughly 230 km s^{-1}).

Numerical simulations of convection in rotating shells (Miesch, Brun & Toomre 2006) have roughly reproduced the overall amplitude of the meridional flow, although in these simulations the meridional flow is highly variable and has a multiple-cell structure. These simulations rely on the presence of a small latitudinal entropy gradient to establish solar-like differential rotation as suggested by Rempel (2005). This gradient is imposed at the base of the convection zone model as an adjustable part of the boundary conditions. The differential rotation in these models is, thus, what in geophysics is called a thermal wind, much like the global atmospheric circulation on Earth is due to the pole-equator temperature difference. In the Sun, the cause for such latitudinal entropy variation is not quite clear, however. Independent of this unsolved question, the fact that the simulations so far appear unable to reproduce the solar differential rotation without an imposed entropy gradient is significant. It implies that models of the Sun's differential rotation based on Λ-effect or anisotropic turbulence formalisms so far are not substantiated by numerical simulations.

8.3. Solar-Cycle Variations

The time-varying component of rotation shows bands of slower and faster rotation (± 10 m s^{-1}) that migrate in latitude with the phase of the solar cycle. This pattern, called torsional oscillations, was first seen in direct Doppler measurements (Howard & Labonte 1980). The torsional oscillations have two branches. At latitudes less than about 45°, the bands of increased and decreased rotation move toward the equator at the same rate as the active latitudes; the active latitudes are located on the poleward side of the fast band. At high latitudes, the bands move toward the poles. Global helioseismology has shown that the torsional oscillations have their maximum amplitude close to the surface, but extend throughout much of the convection zone (e.g., Vorontsov et al. 2002). The torsional oscillations tend to be roughly uniform along contours of constant rotation rate (e.g., Howe et al. 2005). As reviewed by Gizon & Birch (2005), local helioseismology has confirmed many of these results for the shallow component of the torsional oscillations. **Figure 21** shows the time residuals of the zonal flows near the surface (time-distance helioseismology).

In addition, local helioseismology has shown that there are fluctuations, with an amplitude of ± 5 m s^{-1}, in the meridional flow that are associated with the butterfly diagram (this pattern was seen in direct Doppler measurements by Ulrich et al. 1988). As shown in **Figure 21**, near the surface these local fluctuations correspond to flows converging toward the active latitudes (e.g., Gizon & Rempel 2008, González Hernández et al. 2008). The exact depth where these flows change sign is not well known, but at depths of roughly 50 Mm, the component of the meridional flow associated with the torsional oscillations converges toward the active latitudes (e.g., Beck, Gizon & Duvall 2002; Chou & Dai 2001). The contribution of flows around individual active regions to the torsional oscillations and associated meridional flows are discussed in Section 7.

Schüssler (1981) and Yoshimura (1981) suggested that the torsional oscillations may be caused by the Lorentz force associated with migrating dynamo waves. A turbulent mean field dynamo
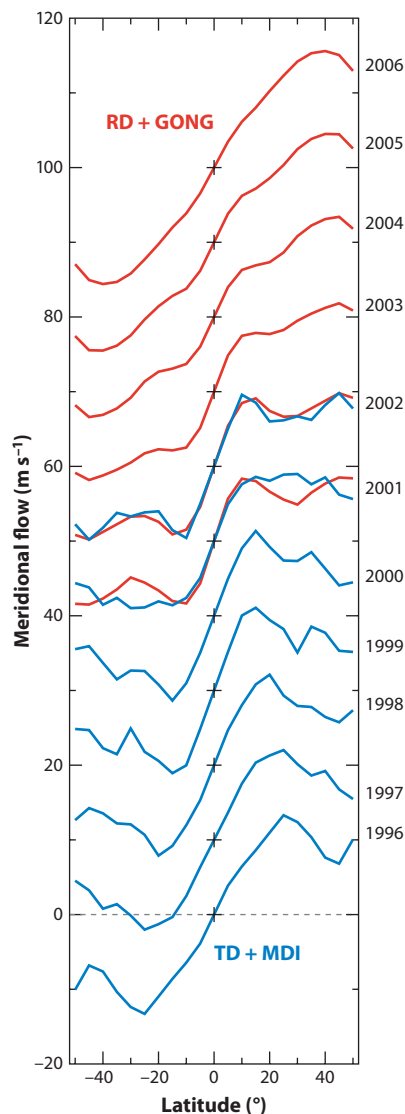
Figure 20

Antisymmetric component of the near-surface meridional flow as a function of latitude during 1996–2006.
Each curve corresponds to a different year as indicated on the right. To improve visibility, years 1997 and
above are shifted by multiples of 10 m s^{-1}. The blue curves until 2002 show the advection of
supergranulation as measured by time-distance helioseismology (Gizon & Rempel 2008) and *Solar and
Heliospheric Observatory*/Michelson Doppler Imager full-disk data (2–3 months per year). The red curves
from 2001 are averages (from the surface down to 7 Mm) of the meridional flow inferred by ring-diagram
(RD) analysis and Global Oscillation Network Group (GONG) data (González Hernández et al. 2008). The
ring-diagram values are multiplied by a factor of 0.8 to ease the comparison. Note the local maximum
moving toward the equator, from 25° in 1996 to 10° in 2006.
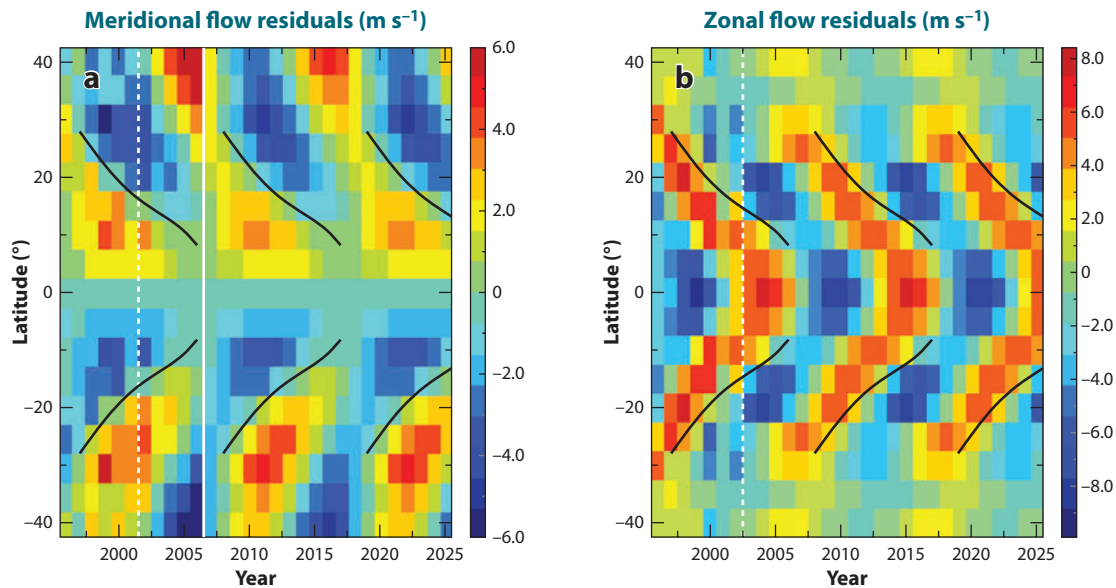
Figure 21

Solar cycle variations of the meridional and zonal flows in the near-surface layers. (*a*) Time residuals of the meridional flow after subtraction of the average meridional flow for 1996–2006 (from **Figure 20**). The color scale is in units of meters per second. The first eleven years (the observations) are extrapolated into the future by fitting the eleven-year periodic component. The thick black curves represent the mean latitude of activity estimated from Mount Wilson magnetograms. (*b*) Time residuals of the zonal flows after subtraction of the mean rotational velocity for the period 1996–2002, followed by the eleven-year periodic component. Flows are deduced from the advection of the supergranulation in *Solar and Heliospheric Observatory/*Michelson Doppler Imager time-distance divergence maps (Gizon & Rempel 2008). The color scale is in units of meters per second.

model by Covas et al. (2000), fitted to a butterfly diagram of the solar cycle, shows a Lorentz force–induced torsional oscillation pattern at the surface resembling the observations. As in other Lorentz-force models, however, its amplitude increases strongly with depth, in contrast with the helioseismic measurements. Kitchatinov et al. (1999), building on work by Küker, Rüdiger & Pipin (1996), suggested that the torsional oscillations result from the effect of the magnetic field on the convective transport of angular momentum. Another suggested explanation is the reduction of turbulent viscosity in active regions (Petrovay & Forgács-Dajka 2002).

Spruit (2003) suggested that the torsional oscillations may be a result of geostrophic flows set up by enhanced surface cooling in regions of magnetic activity. Because the driving force in this explanation is at the surface, the velocity signal produced decreases with depth as observed. Rempel (2007) argued that such a thermal forcing, rather than mechanical forcing as in the Lorentz force–based models, is required to explain the observed deviation of the low-latitude torsional oscillations from a Taylor-Proudman state (zonal velocity constant on cylinders). Similarly, Gizon & Rempel (2008) suggested that the only current model for the low-latitude branch of the torsional oscillations and associated meridional flows that is qualitatively consistent with the observations is the enhanced cooling model of Spruit (2003). One complication for models that invoke thermal forcing at the surface is to explain the presence of the torsional oscillations at solar minimum (Gizon & Rempel 2008). It should be noted that the model of Rempel (2007) does not require enhanced thermal forcing at high latitudes (>50°) to explain the poleward-propagating branch of the torsional oscillations. The two branches of the zonal torsional oscillations may have different physical origins.

8.4. Contribution of Active Region Flows to Longitudinal Averages

An interesting question is whether the localized flows around active regions (Section 7) contribute significantly to the solar-cycle variation of the longitudinal averages of the differential rotation and the meridional flow. The inflows/outflows around active regions could affect the average meridional circulation around the mean latitude of activity, whereas the vortical component of the flows could affect the average zonal flows.

In order to study this question, Gizon (2003) selected all regions within 5° of all locations having a strong magnetic field and excluded these regions from the longitudinal averages of the flows. The resulting zonal flows are essentially unaffected (except for the fact that active regions rotate a little more rapidly than quiet Sun): Localized cyclonic flows around large active regions do not provide a sufficient explanation for the torsional oscillations. This is not particularly surprising because zonal torsional oscillations exist at solar minimum, in the absence of active regions. The torsional oscillations model of Spruit (2003) would have to rely on the thermal disturbances caused by diffuse small-scale magnetic fields, not localized active regions. However, Gizon (2003) finds that the north-south inflows around active regions, when averaged over longitude, provide an explanation for the near-surface solar-cycle dependency of the meridional flow at the level of a few meters per second. This conclusion has been challenged by González Hernández et al. (2008).

9. FARSIDE IMAGING

Lindsey & Braun (2000) introduced the concept of farside imaging, in which observations of the solar oscillations made on the visible disk are used to infer the presence of active regions on the farside of the Sun. Farside imaging has been achieved using both holography-based methods (e.g., Lindsey & Braun 2000) and time-distance helioseismology (Zhao 2007). Hartlep et al. (2008) have successfully tested farside time-distance helioseismology with numerical simulations.

The conceptual ray geometry for farside imaging is shown in **Figure 22a**. In the 2+2 skip geometry, wave packets leave the visible surface, make two skips in the solar interior (this involves one reflection from the surface), interact with possible surface magnetic activity on the farside, make two more skips, and are then seen again on the front side. The total travel time of the wave packet is sensitive to the presence of large active regions on the farside. Travel-time reductions of up to ten seconds are typically observed for large active regions. By moving the farside target location, a map of the farside magnetic activity can be constructed. The 2+2 skip geometry is suitable for mapping regions that are not too far from the antipode of the center of the visible disk. In order to complete the farside maps, other skip geometries are required (Braun & Lindsey 2001). The 1+3 skip geometry targets active regions closer to the limb. In this geometry, the wave packets only skip once before they reach the target location, and then skip three times before they are observed again. K. Oslund and P.H. Scherrer (unpublished data) combined farside maps from the $2 + 2$ and $1 + 3$ skip geometries to make maps of the entire farside of the Sun. These farside maps are produced daily using the SOHO/MDI data and are available online (see Related Resources).

Figure 22b and **Supplemental Videos 9** and **10** show a sequence of farside maps that show a large active region moving across the farside and front side of the Sun. This active region, NOAA 9503, was seen to form on the farside of the Sun before appearing on the visible disk about 12 days later. Magnetic maps of the farside provide up to two weeks of advance warning before large active regions rotate onto the visible disk and, thus, are expected to play an important role in predicting space weather.
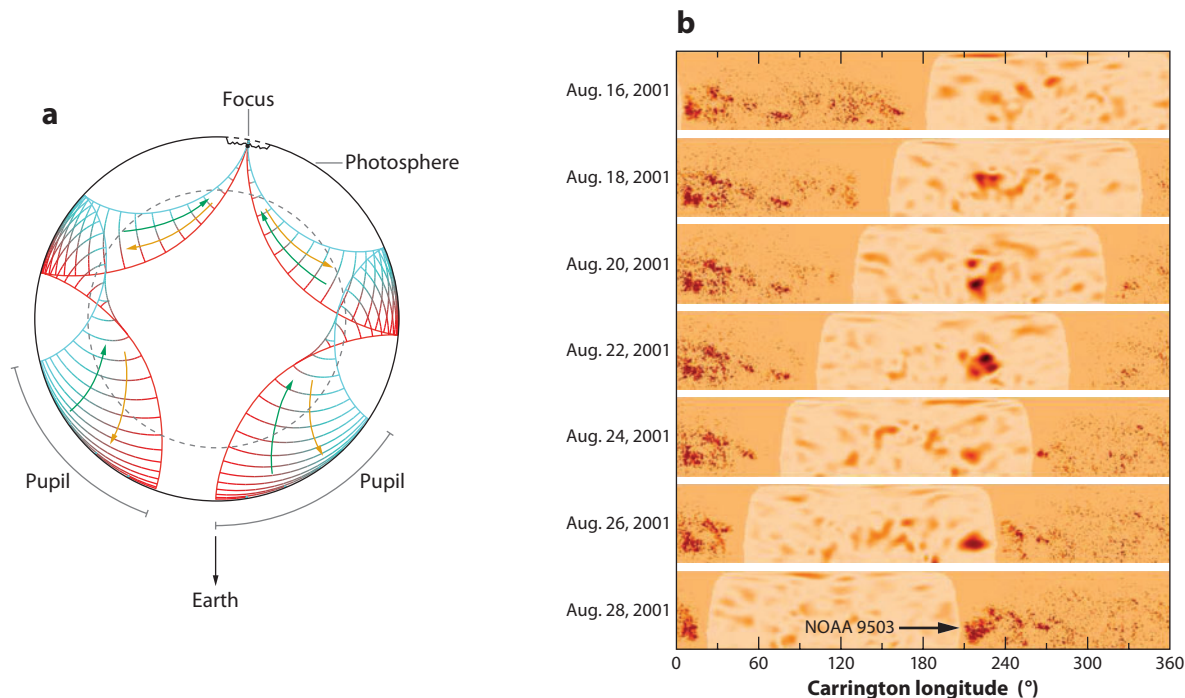
Supplemental Material

a

Focus

Photosphere

Pupil

Pupil

Earth

b

Aug. 16, 2001

Aug. 18, 2001

Aug. 20, 2001

Aug. 22, 2001

Aug. 24, 2001

Aug. 26, 2001

Aug. 28, 2001

NOAA 9503 →

0   60   120   180   240   300   360
Carrington longitude (°)

Figure 22

Farside imaging. (*a*) Ray-path diagram for 2+2 skip farside imaging (Lindsey & Braun 2000). Waves seen leaving (arriving) at the pupils on the visible surface of the Sun travel in the direction of the yellow (green) arrows. The waves skip from the solar surface once before, and once after, reaching the focal point on the farside of the Sun. Active regions located at the focal point induce small phase shifts into the waves. (*b*) Global Oscillation Network Group (GONG) farside images (*lighter yellow background*) combined with magnetograms of the front side (*darker yellow background*) covering a 12-day period each. Each full-Sun map is plotted as a function of Carrington longitude (longitude in a corotating frame) and latitude. The Active Region NOAA 9503 (August 2001) is seen to form on the farside of the Sun and then rotate onto the visible disk. Courtesy of Charles Lindsey.

In order to interpret the farside maps in terms of physical variables, such as the total unsigned magnetic flux, González Hernández, Hill & Lindsey (2007) have proposed to calibrate the farside images using long-lived active regions that are seen before and after they appear on the farside. Future Sun-orbiting spacecraft carrying solar and magnetic imagers (e.g., Solar Orbiter) will provide enhanced opportunities for detailed farside calibration.

10. FLARE-EXCITED WAVES

The excitation of solar oscillations by a flare was first observed by Kosovichev & Zharkova (1998) using MDI data. Since then, many other examples have been found (e.g., Donea et al. 2006). **Figure 23** shows a summary of some observations of the waves generated by the flare of January 15, 2005. In this example, the location of the wave source (as estimated from helioseismic holography) is seen to nearly coincide with the hard x-ray emission as seen by the *Ramaty High-Energy Solar Spectroscopic Imager* (RHESSI) spacecraft. The seismic waves are first seen about 20 minutes after the hard x-ray emission and propagate outward according to the time-distance relation (**Figure 6a**). In addition to exciting local waves, solar flares are also observed to put energy into the very low-degree global modes (Karoff & Kjeldsen 2008).
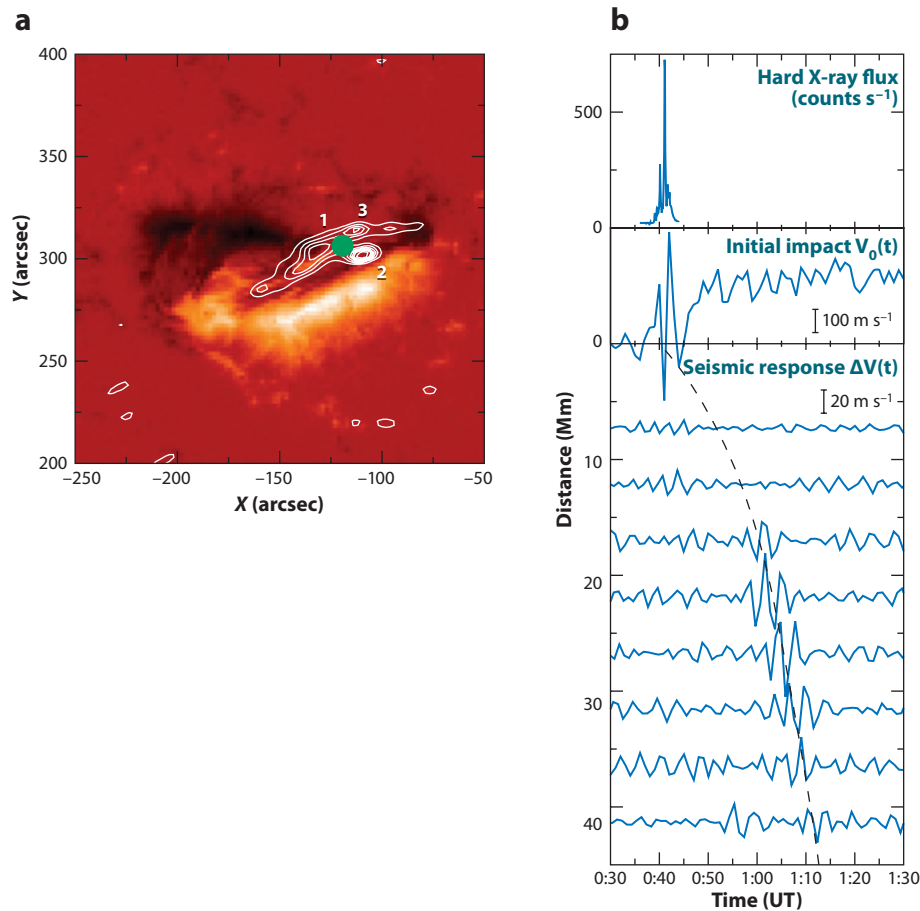
Figure 23

Flare-excited waves in Active Region NOAA 10720 on January 15, 2005. (*a*) *Solar and Heliospheric Observatory*/Michelson Doppler Imager (MDI) magnetogram (*color background*) with *Ramaty High-Energy Solar Spectroscopic Imager* (RHESSI) X-ray emission averaged over the period 00:41:33–00:42:34 UT (12–25 keV contours at 10, 20, 30, 40, 50, 60, and 80 percent of the maximum flux). Three hard X-ray sources are observed. The green dot shows the location of the helioseismic source (Moradi et al. 2007). Courtesy of Alina Donea and Hamed Moradi. (*b*) Sequence of events. High-energy electrons accelerated in the solar flare interact with the lower atmosphere, producing hard X-ray emission (observed by RHESSI) and shocks leading to an initial hydrodynamic impact in the photosphere (observed by MDI). Raw MDI Dopplergrams reveal an expanding seismic wave about 20 min after the initial impact. The dashed curve shows a theoretical time-distance curve for helioseismic waves. Figure and caption from Kosovichev (2006). With kind permission of Springer Science and Business Media.

The details of the physical mechanism responsible for the wave excitation are not clear. Two main suggestions have been high-energy electrons (Kosovichev 2007) and the Lorentz forces (Hudson, Fisher & Welsch 2008) due to the reconfiguration of the magnetic field during the flare. Lindsey & Donea (2008) discuss the competing mechanisms in detail. Additional observations and modeling efforts are needed in order to test these proposals.

11. FUTURE OBSERVATIONS

11.1. Solar Dynamics Observatory

The Helioseismic and Magnetic Imager (HMI) is designed to deliver ideal data for local helioseismology. HMI is one of several instruments onboard NASA's *Solar Dynamics Observatory* (SDO), which was successfully launched on 11 February 2010 in a geosynchronous orbit. HMI will transmit $4,096 \times 4,096$-pixel Doppler images of the Sun at the cadence of one image every 45 s. It will combine high spatial resolution (1 arcsec) and full spatial coverage, with a very high duty cycle over a nominal mission duration of five years. This combination will make possible the local helioseismic analysis of regions closer to the limb (less foreshortening), in order to study higher solar latitudes and the evolution of magnetic active regions as they rotate from limb to limb across the solar disk. In addition to Dopplergrams, HMI will provide images of the three components of the vector magnetic field, providing important information for the interpretation of helioseismic data. A stated goal of SDO/HMI is the subsurface detection of the magnetic field before it emerges at the surface, leading to reliable predictive capability (Kosovichev & HMI Science Team 2007). In combination with observations from the Atmospheric Imaging Assembly (AIA), a set of four SDO telescopes designed to provide an unprecedented view of the lower corona, HMI and local helioseismology will help establish relationships between the internal structure and dynamics of the Sun and the various components of magnetic activity in the solar atmosphere. SDO instruments will generate a total data flow of about 1.5 TB day^{-1}, which represents a real challenge for the ground segment in terms of data storage, processing, and analysis.

The instrumental design of HMI is similar to MDI's, except for the choice of the absorption line. Using a combined Lyot-Michelson filter system, HMI will take five filtergrams across the FeI line at 6173 Å, separated by 69 mÅ (Borrero et al. 2007). This line has a Lande factor $g = 2.5$ and therefore is better suited for the measurement of the vector magnetic field (than e.g., the Ni 6768 line). A picture of the HMI flight model is shown in **Figure 24**.

11.2. Solar Orbiter

Solar Orbiter is the next solar physics mission of the European Space Agency (ESA) and a logical step after SOHO. The target launch date is 2017. Solar Orbiter will use multiple gravity assist maneuvers at Venus and the Earth such that the inclination of the orbit to the ecliptic will incrementally increase during the course of the mission (about 10 years) to reach heliographic latitudes of at least 30°. The elliptical orbit will have a minimum perihelion distance of 0.22 AU. The scientific payload will include a remote sensing package that will deliver 0.5-arcsec pixel images of the solar photosphere (intensity, Doppler velocity, and magnetic field).

Although the exact details of the orbit (and observation windows) are still being discussed, it is clear that Solar Orbiter will offer unique opportunities for helioseismology (Woch & Gizon 2007). First, it will be possible to study the subsurface flows and structure in the polar regions, which is not possible today and is important to understand the solar cycle. Second, Solar Orbiter will enable us to test and apply the concept of stereoscopic helioseismology. Stereoscopic helioseismology combines observations from different vantage points. Solar Orbiter's orbit is particularly interesting as it will offer a large range of spacecraft-Sun-Earth angles. With observations from two widely different viewing angles (Solar Orbiter and another Earth or near-Earth experiment), it becomes possible to consider acoustic ray paths with very large separation distances (see **Figure 6*b***). This is useful in local helioseismology to probe structures deep in the Sun and, in particular, at the bottom of the convection zone.
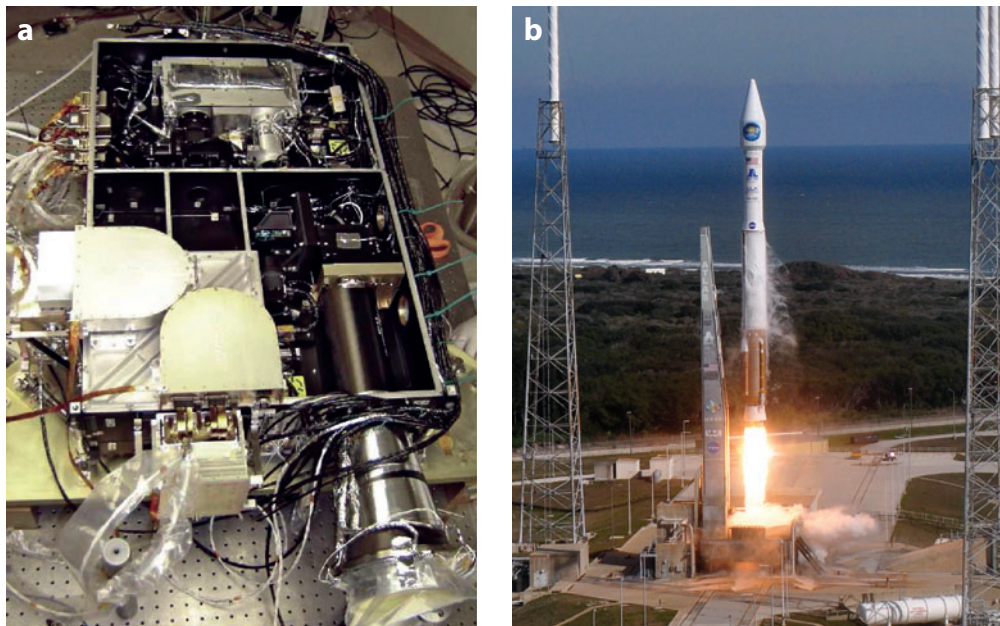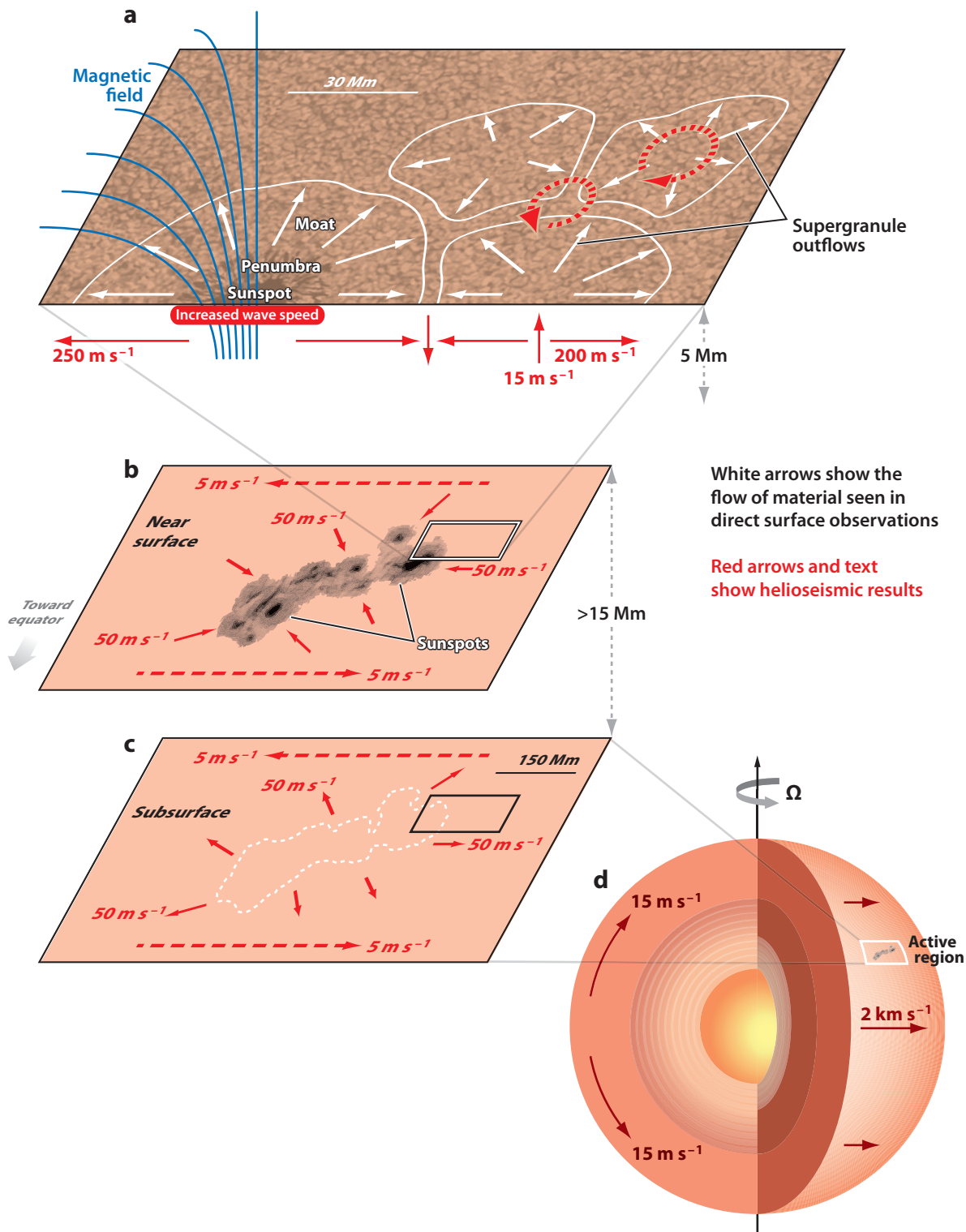
Figure 24

(*a*) The Helioseismic and Magnetic Imager (HMI) instrument onboard NASA's *Solar Dynamics Observatory* (SDO). (*b*) Launch of SDO by an Atlas V rocket from Cape Canaveral on February 11, 2010. At the time of writing, the HMI instrument is going through a commissioning phase and is working with no known issues. Photos courtesy of Philip Scherrer.

12. SUMMARY AND OUTLOOK

Local helioseismology exploits the information contained in the local dispersion relation of the acoustic and surface-gravity waves (ring-diagram analysis) and in the correlations of the random wave field (time-distance helioseismology and related methods) in order to study the subsurface structure and dynamics of the Sun in three dimensions. The high-quality observations from the GONG network and the SOHO satellite have made possible the study of the properties of the upper layers of the convection zone and their variations with the solar cycle.

Local helioseismology has not reached maturity and there are many open questions about data analysis methods and interpretation. The observational results which, in our view, are the most robust and physically sensible are sketched in **Figure 25** and listed in the Summary Points below. Local helioseismology measures effects that are subtle, such as velocities of only a few meters per second. In addition to approximations in the data interpretation, it is important to keep in mind that several sources of instrumental errors can affect the measurements, e.g., plate scale errors and optical distortion (Korzennik, Rabello-Soares & Schou 2004) or uncertainties in the orientation of the image (Giles 2000).

An important challenge for future work in local helioseismology is to detect signatures of magnetic fields at the base of the convection zone, where the field is expected to be amplified by differential rotation and stored until erupting to the surface as active regions. Direct detection through their effect on wave propagation properties is unlikely. Because of the high pressure at the base of the convection zone, the contrast in propagation speed is very much lower than in surface structures like sunspots, even at the inferred field strengths of $\sim 10^5$ G. More promising is the prospect of detecting systematic flows that might be associated with magnetic structures at

a

Magnetic field

30 Mm

Moat

Penumbra

Sunspot

Increased wave speed

250 m s^{-1}

200 m s^{-1}

15 m s^{-1}

Supergranule outflows

5 Mm

b

Near surface

5 m s^{-1}

50 m s^{-1}

50 m s^{-1}

50 m s^{-1}

50 m s^{-1}

Sunspots

5 m s^{-1}

Toward equator

White arrows show the flow of material seen in direct surface observations

Red arrows and text show helioseismic results

>15 Mm

c

Subsurface

5 m s^{-1}

50 m s^{-1}

50 m s^{-1}

50 m s^{-1}

150 Mm

5 m s^{-1}

d

Ω

15 m s^{-1}

15 m s^{-1}

Active region

2 km s^{-1}

the base of the convection zone. Easiest to detect would be azimuthal flows (variations in rotation rate), such as have already been reported on the timescale of the solar cycle. Even if the sensitivity of helioseismic methods turns out to be insufficient to detect such deeply seated structures, it may well be sufficient to rule out certain less-preferred classes of models for the solar cycle, such as convective dynamo models acting throughout the convection zone or in a shallow surface layer. An important class of flows would be the geostrophic flows caused by thermal effects of magnetic fields (see Section 7). Such disturbances are much easier to detect through their thermal winds than directly by their temperature contrast. They might be turned into a diagnostic of magnetic fields in deeper layers that can be probed with helioseismology.

The availability of powerful computers provides exciting opportunities to devise, validate, and optimize improved methods of local helioseismology. Exploring these possibilities will be key to taking full advantage of the observations of solar oscillations. In Sections 4.2 and 6, we have shown examples of the usefulness of numerical simulations of wave propagation through prescribed reference sunspot models. Simulations of wave propagation in spherical geometry (e.g., Hanasoge et al. 2006) have been used in time-distance studies of the deep convection zone (e.g., Zhao et al. 2009) and to validate farside imaging (Hartlep et al. 2008).

It is now becoming possible to simulate the near surface layers of the Sun, including pores and sunspots, by numerically solving the radiative MHD equations (Rempel et al. 2009). **Figure 26a** shows a snapshot of the intensity and the magnetic field for a sunspot simulation. In this simulation, the solar oscillations are naturally excited by the convection (see **Figure 26b**). This type of simulation provides a means for computing realistic time series of Dopplergrams, which can be used as input for all the methods of local helioseismology. With this type of data set, it becomes possible to resolve some of the outstanding issues, for example regarding sunspot subsurface structure (Section 6.4). The recently achieved convergence of observations and realistic 3D radiative MHD simulations of sunspots can count as a major success story in solar physics. It adds confidence in our numerical methods and in our understanding of the physics of solar magnetic activity.

There are many complications in local helioseismology that have not been studied in detail, e.g., instrumental artifacts (point spread function, astigmatism, plate scale), interpretation of the observable (e.g., filtergrams used to construct Dopplergrams) in terms of physical conditions in the solar atmosphere, center-to-limb effects such as foreshortening, and line-of-sight projection of the solar velocity. Other complications are related to the physics of wave propagation, e.g., surface magnetic effects, scattering by time-varying heterogeneities (turbulence), multiple scattering, and physical description of wave excitation and attenuation. Understanding and, in some cases, correcting for these issues is needed to apply local helioseismology to challenging problems: deep meridional circulation (Braun & Birch 2008), detecting subsurface emerging active regions, high latitudes, statistical description of turbulent flows (e.g., Reynolds stresses), etc. In addition,

←--

Figure 25

Summary of local helioseismology results. (*a*) Supergranulation horizontal and vertical flows in the top 5 Mm and associated average Coriolis vorticity in the north (*curved arrows*). The lifetime of the supergranulation pattern is about 2 days. Also shown is the outflow in the sunspot moat and the increased wave speed in the top 1 Mm below the sunspot. (*b*) Extended near-surface inflows around an active region (sunspot group and plage). The dashed red arrows show the zonal shear around the active latitude (± 5 m s^{-1} torsional oscillation). (*c*) Extended outflows around the active region at depths greater than ~ 15 Mm. The zonal shear flow is the same as near the surface. (*d*) Latitudinal differential rotation and poleward meridional flow. The time-varying component of the meridional flow (not plotted) corresponds to a 5-m-s^{-1} inflow toward the mean latitude of activity near the surface (cf. panel *b*) and a 5-m-s^{-1} outflow at greater depths (cf. panel *c*).
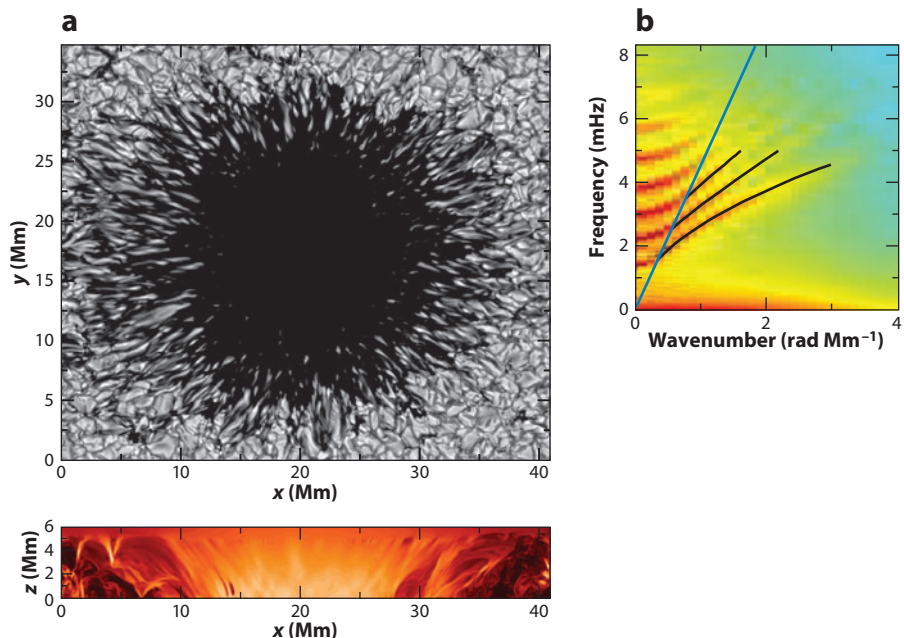
a

b

Figure 26

Radiative magnetohydrodynamic simulation of a sunspot by Rempel et al. (2009). (*a*) Bolometric intensity
(*black and white*) and subsurface magnetic field strength on a vertical cut through the center of the sunspot (in
the range of 0–8 kG). See **Supplemental Video 11**. (*b*) Power spectrum of the surface oscillations in the
simulation. The blue line is the phase speed at the bottom of the box, above which the model is not realistic.

inferring small amplitude perturbations in the solar interior may require many years of observa-
tions and/or appropriate spatial/temporal averaging to optimize signal-to-noise ratios.

Finally, it is worth exploring the many connections between the results of local helioseismology
and global-mode helioseismology: for example, the contribution of active regions to the temporal
variations of low-degree mode frequencies, comparisons of rotation measurements (e.g., 1.3-year
tachocline oscillations), deep sound-speed anomalies (Zhao et al. 2009), and seismic radii (González
Hernández, Scherrer & Hill 2009; Kholikov & Hill 2008). In principle, local helioseismology
should help improve surface boundary conditions for global-mode inversions.

SUMMARY POINTS

1. Local helioseismology shows that supergranules are characterized by horizontal outflows
   of $\sim$200 m s^{-1} and upflows of $\sim$20 m s^{-1} near the surface. Magnetic field concentrations
   are observed at the boundaries of supergranules, and the inclined field provides portals
   through which low-frequency waves propagate into the chromosphere. The correlation
   between the horizontal divergence of the flow and the vertical component of vorticity
   has been measured as a function of latitude: Cyclonic convection is explained by the
   effect of the Coriolis force. The pattern of supergranulation has (unexplained) wave-like
   properties.

2. The amplitudes, phases, and frequencies of the solar waves are strongly affected by sunspots. Sunspots "absorb" a fraction of the ingoing waves as they partially convert into downward propagating slow MHD waves. Sunspots are surrounded by a horizontal outflow (several hundred meters per second) in an annular region extending as far as twice the penumbral radius. This moat flow, which persists at least in the top 4 Mm, is consistent with direct observations of the solar surface. Little is known about the subsurface magnetic and thermal structure of sunspots. Forward modeling of the helioseismic wave field requires a surface field of several kilogauss. Multiheight observations of solar oscillations have been used to map the sunspot magnetic canopy.

3. Local helioseismology has confirmed the latitudinal differential rotation and the increase of rotation with depth in the top ∼35 Mm of the convection zone (near-surface shear layer). Flows in meridional planes have been measured by local helioseismology in the top ∼50 Mm. For latitudes less than 40°, the longitudinal component of the flow is poleward, with a maximum amplitude of 15 m s^{-1}. It is not clear whether the meridional flow can be detected reliably deeper or at higher latitudes.

4. The solar-cycle variation of rotation has been confirmed: Bands of faster and slower rotation (±10 m s^{-1}) migrate in latitude with magnetic activity. In addition, local helioseismology has revealed that the longitudinal average of the meridional flow also varies with the solar cycle (±5 m s^{-1}), i.e., by a significant fraction of its mean value. Near the surface, the time residuals are consistent with a north-south inflow around the mean latitude of activity. At a depth of 50 Mm, the residuals are consistent with a small outflow.

5. On intermediate scales (∼20°) weak horizontal inflows (∼50 m s^{-1}) have been detected around complexes of magnetic activity, near the surface. If confirmed, these flows may explain the time evolution of the longitudinal average of the meridional flow. At greater depths (>10 Mm) the horizontal flows appear to switch sign and diverge from centers of magnetic activity (∼50 m s^{-1}). In addition, the surface inflows are associated with cyclonic vorticity.

6. Farside helioseismology works. Large active regions can be detected on the invisible hemisphere of the Sun, thus providing advanced warning of energetic particle events, days before they occur on the front side.

FUTURE ISSUES

1. The most pressing issue in local helioseismology is how to interpret magnetic effects, which requires new methods of analysis. This is illustrated by the fact that the standard methods of analysis yield conflicting inferences regarding sunspot structure and dynamics (e.g., **Figure 16**). The way forward is to develop methods that incorporate appropriate physical models of the interaction of waves with strong magnetic fields near the surface. Surface magnetic effects must be accounted for before we can detect and study the magnetic field below the photosphere.

2. Instrumental artifacts often dominate realization noise and hamper the study of weak perturbations in the Sun. Ever-improving instrumentation is essential to pushing the limits of local helioseismology, especially to probe the deepest layers of the convection zone and the high-latitude meridional flow. The SDO/HMI instrument, which was recently launched, represents an important technological step toward improved observations.

3. Helioseismology has benefited from methods developed for the seismology of the Earth: normal mode theory, travel-time sensitivity kernels, interpretation of the cross-covariance, inverse methods, etc. We expect that local helioseismology will continue to learn from advances in Earth seismology: Notable progress has been made on numerical simulations of wave propagation, the computation of travel-time sensitivity kernels using numerical methods, and nonlinear inversions of travel times (various aspects of modern seismology are discussed by, e.g., Tape et al. 2009).

DISCLOSURE STATEMENT

The authors are not aware of any affiliations, memberships, funding, or financial holdings that might be perceived as affecting the objectivity of this review.

ACKNOWLEDGMENTS

LITERATURE CITED

Babcock HW. 1961. *Ap. J.* 133:572
Baig AM, Dahlen FA, Hung SH. 2003. *Geophys. J. Int.* 153:467
Basu S, Antia HM, Bogart RS. 2004. *Ap. J.* 610:1157
Basu S, Antia HM, Tripathy SC. 1999. *Ap. J.* 512:458
Beck JG, Gizon L, Duvall TL Jr. 2002. *Ap. J. Lett.* 575:L47
Birch AC. 2008. *J. Phys. Conf. Ser.* 118:012009
Birch AC, Braun DC, Hanasoge SM, Cameron R. 2009. *Sol. Phys.* 254:17
Birch AC, Felder G. 2004. *Ap. J.* 616:1261
Birch AC, Gizon L. 2007. *Astron. Nachr.* 328:228
Birch AC, Gizon L, Hindman BW, Haber DA. 2007. *Ap. J.* 662:730

Birch AC, Kosovichev AG. 2000. *Sol. Phys.* 192:193

Birch AC, Kosovichev AG, Price GH, Schlottmann RB. 2001. *Ap. J. Lett.* 561:L229

Bogdan TJ. 1997. *Ap. J.* 477:475

Bogdan TJ, Cally PS. 1995. *Ap. J.* 453:919

Borrero JM, Tomczyk S, Norton A, Darnell T, Schou J, et al. 2007. *Sol. Phys.* 240:177

Braun DC. 1995. *Ap. J.* 451:859

Braun DC, Birch AC. 2008. *Ap. J. Lett.* 689:L161

Braun DC, Duvall TL Jr, Labonte BJ. 1987. *Ap. J. Lett.* 319:L27

Braun DC, Duvall TL Jr, Labonte BJ. 1988. *Ap. J.* 335:1015

Braun DC, Duvall TL Jr, Labonte BJ, Jefferies SM, Harvey JW, Pomerantz MA. 1992. *Ap. J. Lett.* 391:L113

Braun DC, Lindsey C. 2000. *Sol. Phys.* 192:285

Braun DC, Lindsey C. 2001. *Ap. J. Lett.* 560:L189

Braun DC, Lindsey C. 2003. See Sawaya-Lacoste 2003, p. 15

Brickhouse NS, Labonte BJ. 1988. *Sol. Phys.* 115:43

Busse FH. 2007. *Sol. Phys.* 245:27

Cabrera Solana D, Bellot Rubio LR, Beck C, del Toro Iniesta JC. 2006. *Ap. J. Lett.* 649:L41

Cally PS. 2000. *Sol. Phys.* 192:395

Cally PS. 2007. *Astron. Nachr.* 328:286

Cally PS, Bogdan TJ. 1993. *Ap. J.* 402:721

Cally PS, Bogdan TJ. 1997. *Ap. J. Lett.* 486:L67

Cally PS, Crouch AD, Braun DC. 2003. *MNRAS* 346:381

Cally PS, Goossens M. 2008. *Sol. Phys.* 251:251

Cameron R, Gizon L, Daiffallah K. 2007. *Astron. Nachr.* 328:313

Cameron R, Gizon L, Duvall TL Jr. 2008. *Sol. Phys.* 251:291

Cameron R, Gizon L, Schunker H, Pietarila A. 2010. *Solar Phys.* In press (arXiv 1003.0528)

Chang HK, Chou DY, Labonte BJ, The TON Team. 1997. *Nature* 389:825

Charbonneau P. 2005. *Living Rev. Sol. Phys.* 2:2

Cheung MCM, Schüssler M, Tarbell TD, Title AM. 2008. *Ap. J.* 687:1373

Chou DY, Dai DC. 2001. *Ap. J. Lett.* 559:L175

Chou DY, Sun MT, Huang TY, Lai SP, Chi PJ, et al. 1995. *Sol. Phys.* 160:237

Christensen-Dalsgaard J. 2002. *Rev. Mod. Phys.* 74:1073

Christensen-Dalsgaard J, Dappen W, Ajukov SV, Anderson ER, Antia HM, et al. 1996. *Science* 272:1286

Christensen-Dalsgaard J, Schou J, Thompson MJ. 1990. *MNRAS* 242:353

Colin de Verdière Y. 2006. *Mathematical Models for Passive Imaging. I. General Background.* arxiv.org:math-ph/0610043v1

Couvidat S, Birch AC, Kosovichev AG. 2006. *Ap. J.* 640:516

Couvidat S, Gizon L, Birch AC, Larsen RM, Kosovichev AG. 2005. *Ap. J. Suppl.* 158:217

Covas E, Tavakol R, Moss D, Tworkowski A. 2000. *Astron. Astrophys.* 360:L21

Cowling TG. 1953. In *The Solar System.* Vol. 1: *The Sun*, ed. GP Kuiper, p. 532. Chicago: Univ. Chicago Press

Crouch AD, Cally PS. 2005. *Sol. Phys.* 227:1

Crouch AD, Cally PS, Charbonneau P, Braun DC, Desjardins M. 2005. *MNRAS* 363:1188

Dahlen FA, Hung SH, Nolet G. 2000. *Geophys. J. Int.* 141:157

De Rosa M, Duvall TL Jr, Toomre J. 2000. *Sol. Phys.* 192:351

Dikpati M, Charbonneau P. 1999. *Ap. J.* 518:508

Donea AC, Besliu-Ionescu D, Cally P, Lindsey C. 2006. In *Solar MHD Theory and Observations: A High Spatial Resolution Perspective*, ed. J Leibacher, RF Stein, H Uitenbroek, *ASP Conf. Ser.* 354, p. 204

Duvall TL Jr. 1998. In *Structure and Dynamics of the Interior of the Sun and Sun-like Stars*, ed. S Korzennik, ESA SP 418, p. 581

Duvall TL Jr, D'Silva S, Jefferies SM, Harvey JW, Schou J. 1996. *Nature* 379:235

Duvall TL Jr, Birch AC, Gizon L. 2006. *Ap. J.* 646:553

Duvall TL Jr, Gizon L. 2000. *Sol. Phys.* 192:177

Duvall TL Jr, Jefferies SM, Harvey JW, Pomerantz MA. 1993. *Nature* 362:430

Discusses solar modes, wave packets, and rays.

Discusses mode absorption and mode coupling by sunspots.

Discusses observations and modeling of the cross-covariance around a sunspot.

Duvall TL Jr, Kosovichev AG, Scherrer PH, Bogart RS, Bush RI, et al. 1997. *Sol. Phys.* 170:63

Fan Y, Braun DC, Chou DY. 1995. *Ap. J.* 451:877

Finsterle W, Jefferies SM, Cacciani A, Rapex P, Giebink C, et al. 2004a. *Sol. Phys.* 220:317

Finsterle W, Jefferies SM, Cacciani A, Rapex P, McIntosh SW. 2004b. *Ap. J. Lett.* 613:L185

Galloway DJ, Proctor MRE, Weiss NO. 1977. *Nature* 266:686

Discusses the detection of meridional circulation with time-distance helioseismology.

Giles PM. 2000. *Time-distance measurements of large-scale flows in the solar convection zone*. PhD thesis. Stanford Univ. 144 pp.

Giles PM, Duvall TL Jr, Scherrer PH. 1998. In *Structure and Dynamics of the Interior of the Sun and Sun-like Stars*, ed. S Korzennik, ESA SP 418, p. 775

Giles PM, Duvall TL Jr, Scherrer PH, Bogart RS. 1997. *Nature* 390:52

Gizon L. 2003. *Probing flows in the upper solar convection zone*. PhD thesis. Stanford Univ. 183 pp.

Discusses the forward problem and the first Born approximation.

Gizon L, Birch AC. 2002. *Ap. J.* 571:966

Gizon L, Birch AC. 2004. *Ap. J.* 614:472

Gizon L, Birch AC. 2005. *Living Rev. Sol. Phys.* 2:6 (available at http://solarphysics.livingreviews.org/Articles/lrsp-2005-6/)

Provides a comprehensive open-access review of local helioseismology.

Gizon L, Duvall TL Jr. 2003. See Sawaya-Lacoste 2003, p. 43

Gizon L, Duvall TL Jr, Larsen RM. 2000. *J. Astrophys. Astron.* 21:339

Gizon L, Duvall TL Jr, Larsen RM. 2001. In *IAU Symp. 203: Recent Insights into the Physics of the Sun and Heliosphere: Highlights from SOHO and Other Space Missions*, ed. P Brekke, B Fleck, JB Gurman, p. 189

Gizon L, Duvall TL Jr, Schou J. 2003. *Nature* 421:43

Gizon L, Hanasoge SM, Birch AC. 2006. *Ap. J.* 643:549

Gizon L, Rempel M. 2008. *Sol. Phys.* 251:241

Gizon L, Schunker H, Baldner CS, Basu S, Birch AC, et al. 2009. *Space Sci. Rev.* 144:249

Gizon L, Thompson MJ. 2007. *Astron. Nachr.* 328:204

González Hernández I, Hill F, Lindsey C. 2007. *Ap. J.* 669:1382

González Hernández I, Kholikov S, Hill F, Howe R, Komm R. 2008. *Sol. Phys.* 252:235

González Hernández I, Komm R, Hill F, Howe R, Corbard T, Haber DA. 2006. *Ap. J.* 638:576

González Hernández I, Scherrer P, Hill F. 2009. *Ap. J. Lett.* 691:L87

Gouédard P, Stehly L, Brenguier F, Campillo M, Colin de Verdière Y, et al. 2008. *Geophys. Prospect.* 56:375

Haber DA, Hindman BW, Toomre J, Bogart RS, Hill F. 2001. In *SOHO 10/GONG 2000 Workshop: Helio- and Asteroseismology at the Dawn of the Millennium*, ed. A Wilson, PL Pallé, ESA SP-464, p. 213

Haber DA, Hindman BW, Toomre J, Bogart RS, Thompson MJ, Hill F. 2000. *Sol. Phys.* 192:335

Haber DA, Hindman BW, Toomre J, Thompson MJ. 2004. *Sol. Phys.* 220:371

Hanasoge SM. 2008. *Ap. J.* 680:1457

Hanasoge SM, Larsen RM, Duvall TL Jr, DeRosa ML, Hurlburt NE, et al. 2006. *Ap. J.* 648:1268

Hartlep T, Zhao J, Mansour NN, Kosovichev AG. 2008. *Ap. J.* 689:1373

Harvey J, The GONG Instrum. Team. 1995. In *GONG 1994. Helio- and Astro-Seismology from the Earth and Space*, ed. RK Ulrich, EJ Rhodes Jr, W Dappen, *ASP Conf. Ser.* 76, p. 432

Harvey JW, Hill F, Hubbard R, Kennedy JR, Leibacher JW, et al. 1996. *Science* 272:1284

Hathaway DH. 1996. *Ap. J.* 460:1027

Hathaway DH, Beck JG, Han S, Raymond J. 2002. *Sol. Phys.* 205:25–38

Hathaway DH, Nandy D, Wilson RM, Reichmann EJ. 2003. *Ap. J.* 589:665

Hathaway DH, Williams PE, Cuntz M. 2006. *Ap. J.* 644:598

Heinemann T, Nordlund Å, Scharmer GB, Spruit HC. 2007. *Ap. J.* 669:1390

Hill F. 1988. *Ap. J.* 333:996

Hill F. 1989. *Ap. J. Lett.* 343:L69

Hindman BW, Gizon L, Duvall TL Jr, Haber DA, Toomre J. 2004. *Ap. J.* 613:1253

Howard R, Labonte BJ. 1980. *Ap. J. Lett.* 239:L33

Howe R, Christensen-Dalsgaard J, Hill F, Komm R, Schou J, Thompson MJ. 2005. *Ap. J.* 634:1405

Hudson HS, Fisher GH, Welsch BT. 2008. In *Subsurface and Atmospheric Influences on Solar Activity*, ed. R Howe, RW Komm, KS Balasubramaniam, GJD Petrie, *ASP Conf. Ser.* 383, p. 221

Hung SH, Dahlen FA, Nolet G. 2000. *Geophys. J. Int.* 141:175

Hung SH, Dahlen FA, Nolet G. 2001. *Geophys. J. Int.* 146:289

Jackiewicz J, Gizon L, Birch AC. 2008. *Sol. Phys.* 251:381

Jackiewicz J, Gizon L, Birch AC, Duvall TL Jr. 2007. *Ap. J.* 671:1051

Jacobsen BH, Moller I, Jensen JM, Efferso F. 1999. *Phys. Chem. Earth* 24:215

Jefferies SM, McIntosh SW, Armstrong JD, Bogdan TJ, Cacciani A, Fleck B. 2006. ***Ap. J. Lett.*** **648:L151**

Jensen JM, Duvall TL Jr, Jacobsen BH, Christensen-Dalsgaard J. 2001. *Ap. J. Lett.* 553:L193

Jensen JM, Jacobsen BH, Christensen-Dalsgaard J. 2000. *Sol. Phys.* 192:231

Karoff C, Kjeldsen H. 2008. *Ap. J. Lett.* 678:L73

Kholikov S, Hill F. 2008. *Sol. Phys.* 251:157

Khomenko E, Collados M. 2006. *Ap. J.* 653:739

Kitchatinov LL, Pipin VV, Makarov VI, Tlatov AG. 1999. *Sol. Phys.* 189:227

Komm R, Corbard T, Durney BR, González-Hernández I, Hill F, et al. 2004. ***Ap. J.*** **605:554**

Komm R, Howe R, Hill F. 2006. *Adv. Space Res.* 38:845

Komm R, Howe R, Hill F, Miesch M, Haber D, Hindman B. 2007. *Ap. J.* 667:571

Komm RW, Howard RF, Harvey JW. 1993a. *Sol. Phys.* 145:1

Komm RW, Howard RF, Harvey JW. 1993b. *Sol. Phys.* 147:207

Korzennik SG, Rabello-Soares MC, Schou J. 2004. *Ap. J.* 602:481

Kosovichev AG. 1996. *Ap. J. Lett.* 461:L55

Kosovichev AG. 2006. *Sol. Phys.* 238:1

Kosovichev AG. 2007. *Ap. J. Lett.* 670:L65

Kosovichev AG. 2008. *Adv. Space Res.* 41:830

Kosovichev AG, Duvall TL Jr. 1997. In *SCORe'96: Solar Convection and Oscillations and Their Relationship*, ed. FP Pijpers, J Christensen-Dalsgaard, CS Rosenthal, *Ap. Space Sci. Libr.* 225, p. 241

Kosovichev AG, Duvall TL Jr, Birch AC, Gizon L, Scherrer PH, Zhao J. 2002. *Adv. Space Res.* 29:1899

Kosovichev AG, Duvall TL Jr, Scherrer PH. 2000. ***Sol. Phys.*** **192:159**

Kosovichev AG, HMI Sci. Team. 2007. *Astron. Nachr.* 328:339

Kosovichev AG, Zharkova VV. 1998. *Nature* 393:317

Küker M, Rüdiger G, Pipin VV. 1996. *Astron. Astrophys.* 312:615

Larose E, Margerin L, Derode A, van Tiggelen B, Campillo M, et al. 2006. *Geophysics* 71:11

Leibacher JW, Stein RF. 1971. *Ap. Lett.* 7:191

Leighton RB. 1969. *Ap. J.* 156:1

Leighton RB, Noyes RW, Simon GW. 1962. *Ap. J.* 135:474

Lindsey C, Braun DC. 1997. *Ap. J.* 485:895

Lindsey C, Braun DC. 2000. ***Science*** **287:1799**

Lindsey C, Braun DC, Jefferies SM, Woodard MF, Fan Y, et al. 1996. *Ap. J.* 470:636

Lindsey C, Donea A. 2008. *Sol. Phys.* 251:627

Maltby P, Avrett EH, Carlsson M, Kjeldseth-Moe O, Kurucz RL, Loeser R. 1986. *Ap. J.* 306:284

Marquering H, Dahlen FA, Nolet G. 1999. *Geophys. J. Int.* 137:805

Miesch MS. 2005. *Living Rev. Sol. Phys.* 2:1

Miesch MS, Brun AS, Toomre J. 2006. *Ap. J.* 641:618

Mitra-Kraev U, Kosovichev AG, Sekii T. 2008. *Astron. Astrophys.* 481:L1

Montelli R, Nolet G, Dahlen FA, Masters G, Engdahl ER, Hung SH. 2004. *Science* 303:338

Moradi H, Donea AC, Lindsey C, Besliu-Ionescu D, Cally PS. 2007. *MNRAS* 374:1155

Nye A, Bruning D, Labonte BJ. 1988. *Sol. Phys.* 115:251

Parchevsky KV, Kosovichev AG. 2009. *Ap. J.* 694:573

Parker EN. 1979. *Cosmical Magnetic Fields: Their Origin and Their Activity*. New York: Oxford Univ. Press. 860 pp.

Petrovay K, Forgács-Dajka E. 2002. *Sol. Phys.* 205:39

Rempel M. 2005. *Ap. J.* 622:1320

Rempel M. 2007. *Ap. J.* 655:651

Rempel M. 2008. *J. Phys. Conf. Ser.* 118:012032

Rempel M, Schüssler M, Cameron RH, Knölker M. 2009. *Science* 325:171

Discusses multiheight observations of solar oscillations and magnetic portals.

Provides a ring-diagram analysis of subsurface flows.

Reviews time-distance helioseismology.

Discusses imaging active regions on the farside of the Sun.

Sawaya-Lacoste H, ed. 2003. *Proc. SOHO 12/GONG+ 2002. Local and Global Helioseismology: the Present and Future*, ESA SP 517

Scherrer PH, Bogart RS, Bush RI, Hoeksema JT, Kosovichev AG, et al. 1995. *Sol. Phys.* 162:129–88

Schou J, Antia HM, Basu S, Bogart RS, Bush RI, et al. 1998. *Ap. J.* 505:390

Schou J, Bogart R. 1998. *Ap. J. Lett.* 504:L131

Schunker H, Cally PS. 2006. *MNRAS* 372:551

Schüssler M. 1981. *Astron. Astrophys.* 94:L17

Schüssler M, Caligari P, Ferriz-Mas A, Moreno-Insertis F. 1994. *Astron. Astrophys.* 281:L69

Schüssler M, Schmitt D. 2004. *Astron. Astrophys.* 421:349

Shapiro NM, Campillo M, Stehly L, Ritzwoller MH. 2005. *Science* 307:1615

Sheeley NR Jr. 1972. *Sol. Phys.* 25:98

Solanki SK. 2003. *Astron. Astrophys. Rev.* 11:153

Spruit HC. 1997. *Mem. Soc. Astron. Ital.* 68:397

Spruit HC. 2003. *Sol. Phys.* 213:1

Spruit HC, Bogdan TJ. 1992. *Ap. J. Lett.* 391:L109

Švanda M, Zhao J, Kosovichev AG. 2007. *Sol. Phys.* 241:27

Tape C, Liu Q, Maggi A, Tromp J. 2009. *Science* 325:988

Thomas JH, Weiss NO. 2008. *Sunspots and starspots*. Cambridge: Cambridge Univ. Press, 275 pp.

Thompson MJ, Christensen-Dalsgaard J, Miesch MS, Toomre J. 2003. *Annu. Rev. Astron. Astrophys.* 41:599

Thompson MJ, Zharkov S. 2008. *Sol. Phys.* 251:225

Ulrich RK. 1970. *Ap. J.* 162:993

Ulrich RK, Boyden JE, Webster L, Padilla SP, Snodgrass HB. 1988. *Sol. Phys.* 117:291

Vorontsov SV, Christensen-Dalsgaard J, Schou J, Strakhov VN, Thompson MJ. 2002. *Science* 296:101

Weaver RL, Lobkis OI. 2001. *Phys. Rev. Lett.* 87:134301

Woch J, Gizon L. 2007. *Astron. Nachr.* 328:362

Woodard MF. 2002. *Ap. J.* 565:634

Woodard MF. 2007. *Ap. J.* 668:1189

Woodard MF. 2009. *Ap. J. Lett.* 706:L62

Yoshimura H. 1981. *Ap. J.* 247:1102

Zhao J. 2007. *Ap. J. Lett.* 664:L139

Zhao J, Hartlep T, Kosovichev AG, Mansour NN. 2009. *Ap. J.* 702:1150

Zhao J, Kosovichev AG. 2003. See Sawaya-Lacoste 2003, p. 417

Zhao J, Kosovichev AG. 2004. *Ap. J.* 603:776

RELATED RESOURCES

Instrument Web sites: GONG web site at **http://gong.nso.edu/**, SOHO/MDI at **http://soi.stanford.edu/**, and SDO/HMI at **http://hmi.stanford.edu**.

MDI Farside Graphics Viewer at **http://soi.stanford.edu/data/full_farside/farside.html**.

European Helio- and Asteroseismology Network (HELAS) local helioseismology web site at **http://www.mps.mpg.de/projects/seismo/NA4/**. Software tools and selected data sets.

Duvall TL Jr, Harvey JW, Kosovichev AG, Svestka Z, eds. 2000. Topical Issue "Helioseismic Diagnostics of Solar Convection and Activity", *Sol. Phys.* 192(1–2):1–494. Table of contents available at **http://www.springerlink.com/content/h4bhbw3vdj8n/**.

Gizon L, Cally P, Leibacher J. 2008. Topical Issue "Helioseismology, Asteroseismology, and MHD Connections", *Sol. Phys.* 251(1–2):1–666. Table of contents available at **http://www.springerlink.com/content/x548678p1725/**.

Contents

Indexes

Errata

An online log of corrections to *Annual Review of Astronomy and Astrophysics* articles may
be found at http://astro.annualreviews.org/errata.shtml